Asian Power Electronics Journal

First edition April 2020 Printed in Hong Kong by Reprographic Unit.
The Hong Kong Polytechnic University

Disclaimer
Any opinions, findings, conclusions, or recommendations expressed in this material/event do not reflect the views of The Hong Kong Polytechnic University

Table of Content

Comparative Studies on the Primary-Side Frequency and Phase Shift Control for Series-Series Compensated Inductive Power Transfer

Lit Hong Chan[1], Yun Yang[2], Ka-wai Eric Cheng[3]

1. Department of Electrical Engineering, The Hong Kong Polytechnic University, Hong Kong, kenchan1012@gmail.com.
2. Department of Electrical Engineering, The Hong Kong Polytechnic University, Hong Kong, yun1989.yang@polyu.edu.hk.
3. Department of Electrical Engineering, The Hong Kong Polytechnic University, Hong Kong, eric-cheng.cheng@polyu.edu.hk.

Abstract–Since the Society of Automobile Engineers (SAE) launched the guideline J2954 for wireless battery charging of electric vehicles (EVs), research activities on inductive power transfer (IPT) or wireless power transfer (WPT) in EVs are intensified over the last few years. The guideline J2954 calls for an operating frequency around 85 kHz and power at four levels. In this paper, both frequency and phase shift control, are designed by controlling the front-end inverters to achieve constant current (CC) and constant voltage (CV) control of Li-ion battery loads in a power-scaled-down (i.e., 200 W) IPT system. Simulation results using PSIM9.0 have verified the effectiveness of both control strategies.

Keywords-Inductive power transfer (IPT), efficiency, frequency control, phase shift control.

I. INTRODUCTION

Due to the convenience and safety, inductive power transfer (IPT) technology is gaining increasing attentions in recent years and has been widely used for portable electronics, electric vehicles (EVs), and implantable biomedical devices [1]-[3]. Thereinto, the Li-ion batteries are most widely adopted energy storages for IPT systems. Generally, the charging strategy for the Li-ion batteries comprise a constant current (CC) charging first and then a constant voltage (CV) second to prevent the degradation of the lifespans. Specifically, the Li-ion batteries are recommended to be charged in the CC mode when the state-of-charge (SoC) or the output voltage is below a threshold (e.g., 90% or 4.2 V). However, when the SoC or the output voltage is above the threshold, the Li-ion batteries are required to be charged in the CV mode. By far, various efforts have been made to achieve the CC and CV charging [4]-[15]. In [4]-[6], DC-DC converters are used at the receiver sides to implement the CC and CV charging. However, extra power losses are inevitable, which result in reduced efficiencies and large volumes. In [7]-[15], front-end control methods based on the communication-free observers at the primary sides are proposed. The front-end controllers can accurately control the output currents and the output voltages at the nominal conditions, while the robustness of the proposed controllers is quite low. To address these issues, two feedback control, i.e., frequency and phase shift control, are the most reliable and efficient control strategies for the CC and CV charging of battery loads in IPT systems [4], [7].

Frequency control is achieved by regulating the switching frequency of the primary-side inverter based on the feedbacks of the charging current and the charging voltage of the battery load. By changing the switching frequency, the impedances of both the transmitting and the receiving resonators can be altered. As a result, the charging current and the charging voltage can be regulated. Phase shift control is implemented by delaying an angle between the two bridge arms. By changing the phase shift angle, the fundamental component of the input voltage of the transmitter can be altered. Consequently, the charging current and the charging voltage can be regulated. The prominent advantage of the phase shift control is that the IPT system can always be operated at the resonant frequency.

This paper aims to implement both frequency and phase shift control for series-series (SS)-compensated IPT systems. Based on comprehensive analysis of the systems with different mutual inductances and load conditions, simulations are carried out in PSIM9.0 to exhibit the applications of both control strategies for an 85kHz IPT system with the power rating about 200 W. Nevertheless, the control designs are also validated for general IPT systems.

II. ANALYSIS OF THE FREQUENCY AND PHASE SHIFT CONTROL

The circuit diagram of an SS-compensated IPT system with feedback control is depicted in Fig. 1. The input DC voltage is V_{dc}. A full-bridge inverter is adopted to drive the transmitter resonator. Both C_p and C_s are designed in resonances with L_p and L_s as

$$\omega^2 = \frac{1}{L_p C_p} = \frac{1}{L_s C_s} \tag{1}$$

where ω is the switching angular frequency. At the receiver side, a diode-bridge rectifier and a filter capacitor C_f are adopted to feed DC current and voltage for the battery load. Without using a DC regulator at the user-end, the power density, reliability and cost of the receiver circuit can be improved. However, to regulate the charging current in the CC mode and the charging voltage in the CV mode, wired or wireless communications are required between the transmitter and receiver. As shown in Fig. 1, the measured output current (i.e., I_o) and output voltage (i.e., V_o) are fed back to the primary-side controller to regulate the front-end inverter.

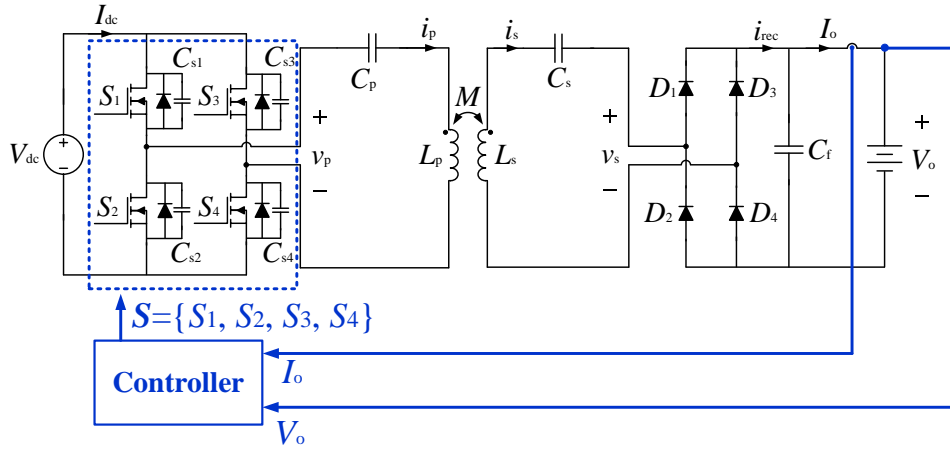Authors *et al*: Guidelines for Preparation of a Paper

Fig. 1: An SS-compensated IPT system with direct feedback control.

Generally, two types of controllers (i.e., frequency and phase shift control) are most widely adopted for the inverters of IPT systems. Based on the circuit diagram in Fig. 1, the equivalent circuit at the fundamental frequency of the system can be plotted, as shown in Fig. 2. Due to the filtering by the resonators, only the fundamental components v_{p1}, i_{p1}, v_{s1} and i_{s1} are considered in the equivalent circuit. Based on the Kirchhoff's circuit laws,

$$v_{p1} = Z_p i_{p1} - j\omega M i_{s1} \qquad (2.1)$$
$$j\omega M i_{p1} = (Z_s + R'_L) i_{s1} \qquad (2.2)$$

where $Z_p = j\omega L_p + \frac{1}{j\omega C_p} + R_p$ and $Z_s = j\omega L_s + \frac{1}{j\omega C_s} + R_s$. R_p and R_s are the equivalent-series-resistances (ESRs). M is the mutual inductance. R'_L is the equivalent resistance of the rectifier, filter (i.e., C_f), and the battery. During the charging process, the battery load can be modelled as a resistive load R_L. Based on the Fourier analysis,

$$R'_L = \frac{8}{\pi^2} R_L \qquad (3)$$

By substituting (3) into (2.2) and eliminating i_{p1} in both (2.1) and (2.2), the charging current and charging voltage of the equivalent circuit, i.e., i_{s1} and v_{s1}, can be derived as

$$i_{s1} = \frac{\pi^2 \omega M}{\pi^2 (Z_p Z_s + \omega^2 M^2) + 8 Z_p R_L} v_{p1} j \qquad (4.1)$$
$$v_{s1} = \frac{8 \omega M R_L}{\pi^2 (Z_p Z_s + \omega^2 M^2) + 8 Z_p R_L} v_{p1} j \qquad (4.2)$$
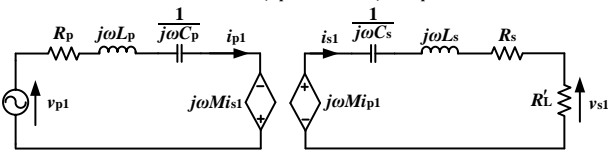
Fig. 2: Equivalent circuit at fundamental frequency.

A. Frequency Control

For the frequency control, the switching signals S_1 and S_2, S_3 and S_4 are complimentary and the switching signals S_1 and S_4, S_2 and S_3 are in phase. The timing diagrams of the four gate signals are depicted in Fig. 3.
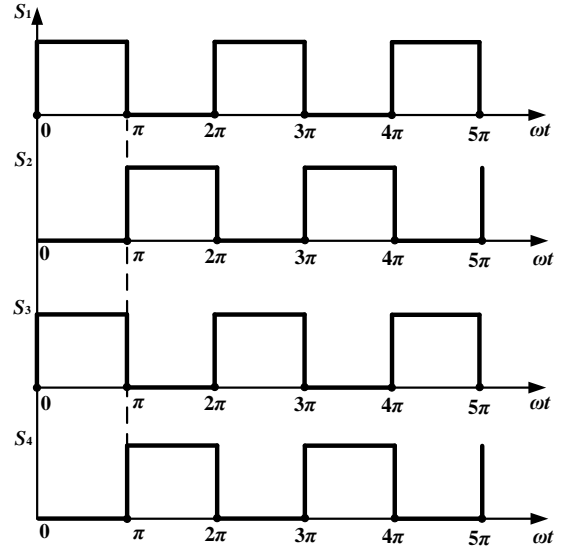
Fig. 3: Timing diagrams of the gate signals of the frequency control.

Therefore, based on the Fourier analysis,

$$I_{p1} = \frac{\pi}{2} I_{dc} \qquad (5.1)$$
$$V_{p1} = \frac{4}{\pi} V_{dc} \qquad (5.2)$$

where V_{p1} and I_{p1} are the peak values of v_{p1} and i_{p1}, respectively. Similarly, the charging current and charging voltage can be derived as

$$I_{s1} = \frac{\pi}{2} I_o \qquad (6.1)$$
$$V_{s1} = \frac{4}{\pi} V_o \qquad (6.2)$$

By substituting (5.2), (6.1) and (6.2) into (4.1) and (4.2), respectively,

$$I_o = \left| \frac{8 \omega M V_{dc}}{\pi^2 (Z_p Z_s + \omega^2 M^2) + 8 Z_p R_L} \right| \qquad (7.1)$$
$$V_o = \left| \frac{8 \omega M R_L V_{dc}}{\pi^2 (Z_p Z_s + \omega^2 M^2) + 8 Z_p R_L} \right| \qquad (7.2)$$

Apparently, the output charging current and the output charging voltage can be regulated by the switching angular frequency ω.
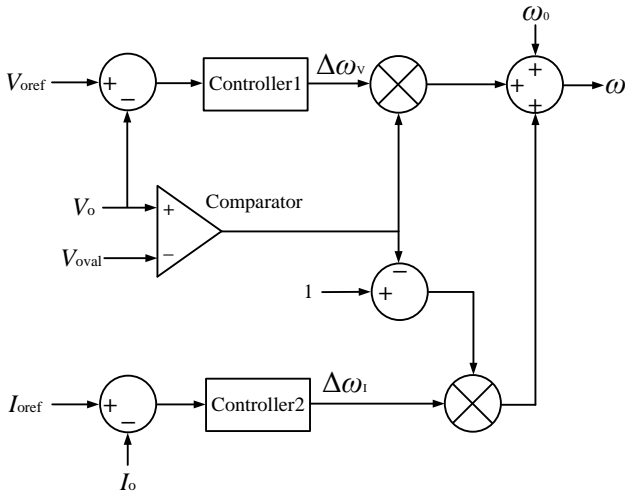
Fig. 4: Schematic diagram of the frequency control.

The schematic diagram of the frequency control is depicted in Fig. 4. Here, V_{oref} and I_{oref} are the output voltage and output current references. The controller1 and controller2 are used to track the voltage and current references, respectively. The outputs of the controller1 and controller2 are $\Delta\omega_V$ and $\Delta\omega_I$, respectively. The output of the frequency control is the addition of $\Delta\omega_V$, $\Delta\omega_I$ and ω_0, where ω_0 is the nominal angular frequency. When V_o is below the threshold (i.e. V_{oval}), the controller2 operates at the CC charging mode, such that the output of the comparator is null. Thus, the output of the frequency control only comprises $\Delta\omega_I$ and ω_0. Similarly, when the battery voltage (i.e., V_o) is above the threshold (i.e. V_{oval}), the controller1 operates at the CV charging mode, such that the output of the comparator is one. Therefore, the output of the frequency control only comprises $\Delta\omega_V$ and ω_0.

B. Phase Shift Control

For the phase shift control, the output current and the output voltage are controlled by changing the phase shift angle between the switching signals S_1 and S_4, S_2 and S_3, while S_1 and S_2, S_3 and S_4 are complimentary. The timing diagrams of the four gate signals are depicted in Fig. 5.
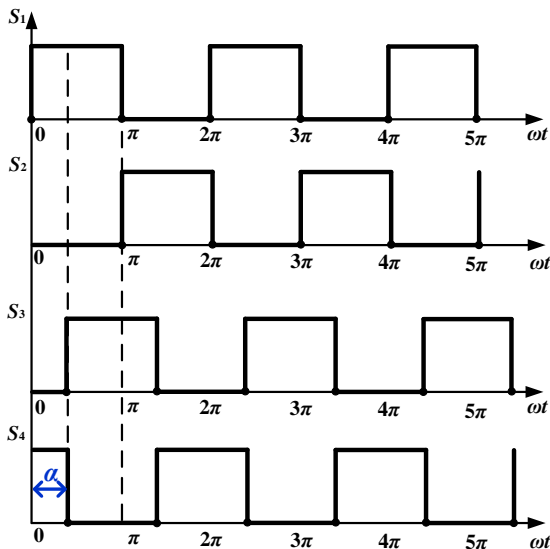

Fig. 5: Timing diagrams of the gate signals of the phase shift control.

Based on the Fourier analysis,

$$V_{p1} = \frac{4}{\pi} V_{dc} \cos\left(\frac{\alpha}{2}\right) \tag{8}$$

By substituting (6.1), (6.2) and (8) into (4.1) and (4.2), respectively,

$$I_o = \left| \frac{8\omega M V_{dc} \cos\left(\frac{\alpha}{2}\right)}{\pi^2 (Z_p Z_s + \omega^2 M^2) + 8 Z_p R_L} \right| \tag{9.1}$$

$$V_o = \left| \frac{8\omega M R_L V_{dc} \cos\left(\frac{\alpha}{2}\right)}{\pi^2 (Z_p Z_s + \omega^2 M^2) + 8 Z_p R_L} \right| \tag{9.2}$$

Apparently, the output current and the output voltage can be regulated by the phase shift angle α.
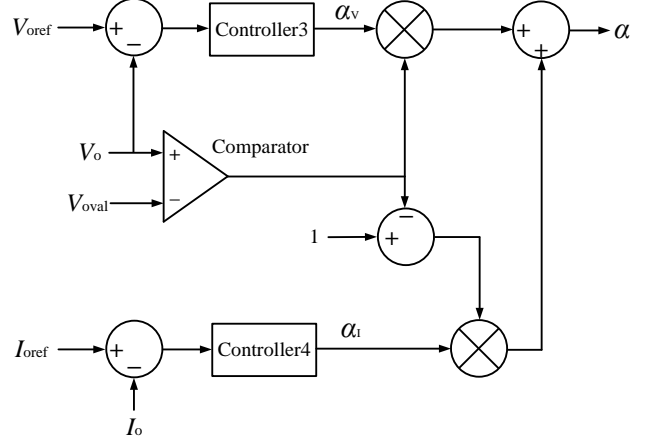
Fig. 6: Schematic diagram of the phase shift control.

The schematic diagram of the phase shift control is depicted in Fig. 6. The outputs of the controller3 and controller4 are α_V and α_I, respectively. The output of the phase control is the addition of α_V and α_I. When the battery voltage (i.e., V_o) is below the threshold (i.e. V_{oval}), the controller4 operates at the CC charging mode, such that the output of the comparator is null. Thus, the output of the phase shift control is α_I. Similarly, when the battery voltage (i.e., V_o) is above the threshold (i.e. V_{oval}), the controller3 operates at the CV charging mode, such that the output of the comparator is one. Thus, the output only comprises α_V and α_I.

III. SIMULATION RESULTS

The parameters of the IPT system in simulation (PSIM9.0) are listed in Table I. The current control and voltage control of both control strategies (i.e., Controller1, Controller2, Controller3, and Controller4) in Figs. 4 and 6 are implemented by proportional-integral (PI) control. The control parameters are given in Table II. The nominal charging current and charging voltage are 12 A and 60 V, respectively.

Table 1: Specifications of the IPT system in simulation

Parameter	Symbol	Value
Nominal frequency	f_0	85 kHz
DC voltage source	V_{dc}	132 V
Parasitic capacitances of the inverter switches	C_{s1}, C_{s2}, C_{s3}, C_{s4}	315 pF
Transmitter coil inductance	L_p	91.78 μH
Receiver coil inductance	L_s	92.05 μH
Transmitter compensated capacitance	C_p	49 nF
Receiver compensated capacitance	C_s	49 nF

ESR of the transmitter	R_p	0.7 Ω
ESR of the Receiver	R_s	0.8 Ω
Forward voltage of the diode in the rectifier	V_D	0.5 V
Filter capacitance	C_f	100 μF
Nominal battery load equivalent resistance	R_L	5 Ω
Nominal mutual inductance	M	19.34 μH

Table 2: Parameters of the controllers

Parameter	Symbol	Value
Proportional gain of Controller1	K_{p1}	-40
Integral gain of Controller1	K_{i1}	-800000
Proportional gain of Controller2	K_{p2}	-28.5
Integral gain of Controller2	K_{i2}	-233128.8
Proportional gain of Controller3	K_{p3}	-4.5
Integral gain of Controller3	K_{i3}	-6923.1
Proportional gain of Controller4	K_{p4}	-16
Integral gain of Controller4	K_{i4}	-38095.2

For the frequency current control, the output current reference is changed from 12 A to 15 A at 0.015 s and changed from 15 A to 10 A at 0.025 s. Fig. 7 shows the waveforms of the output charging current and the switching frequency. Besides, for the frequency voltage control, the reference of the output charging voltage is changed from 60 V to 55 V at 0.015 s and changed from 55 V to 65 V at 0.025 s. Fig. 8 shows the waveforms of the output charging voltage and the switching frequency. Apparently, by changing the operating frequency to be 87.08 kHz, 85.82 kHz and 87.83 kHz at steady states for the current control and 87.14 kHz, 87.55 kHz and 86.72 kHz at steady states for the voltage control, the output charging current and the output charging voltage are well-regulated to track the references. However, the frequency control may suffer from small oscillations at steady state.
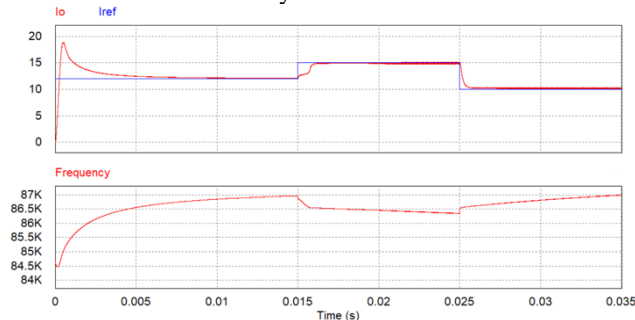
Fig. 7: Output current and switching frequency of the IPT system controlled by the frequency current control.
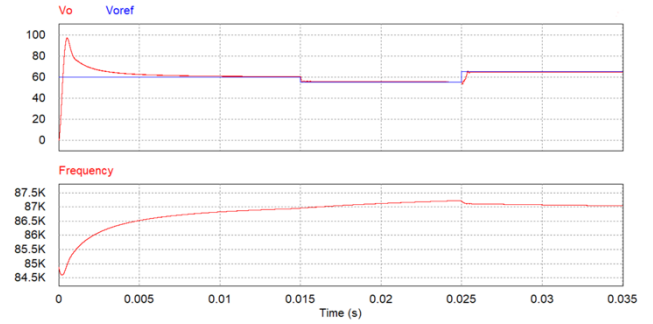
Fig. 8: Output voltage and switching frequency of the IPT system controlled by the frequency voltage control.

For the phase shift current control, the output current reference is also changed from 12 A to 15 A at 0.015 s and changed from 15 A to 10 A at 0.025 s. Fig. 9 shows the waveforms of the output charging current and the corresponding phase shift angle. Besides, for the phase shift voltage control, the reference of output charging voltage is also changed from 60 V to 55 V at 0.015 s and changed from 55 V to 65 V at 0.025 s. The waveforms of the output charging voltage and the corresponding switching frequency are shown in Fig. 10. Obviously, the output charging current and the output charging voltage are well-regulated to track the references by changing the phase shift angle to be -264.7°, -294.9° and -248.8° at steady states for the current control and -265.1°, -256.6° and -273.5° at steady states for the voltage control.
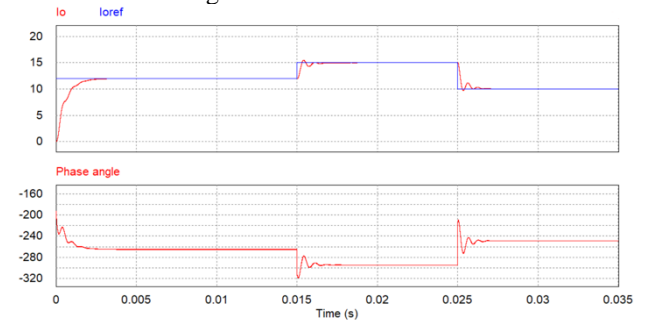
Fig. 9: Output current and shifted angle of the IPT system controlled by the phase shift current control.
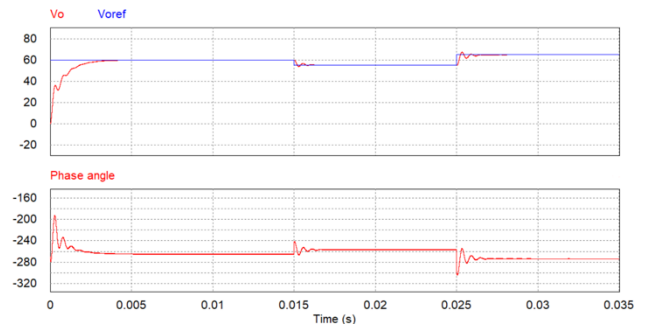
Fig. 10: Output voltage and shifted angle of the IPT system controlled by the phase shift voltage control.

IV. CONCLUSIONS

In this paper, both frequency and phase shift control are deigned to charge the Li-ion battery loads of SS-compensated IPT systems in the CC and CV modes. Simulations are carried out in PSIM9.0 to validate that both control strategies can effectively regulate the output charging current and the output charging voltage of a 85 kHz and 200 W IPT system with different charging current and charging voltage references.

REFERENCES

[1] C. C. Mi, G. Buja, S. Y. Choi and C. T. Rim, "Modern advances in wireless power transfer systems for roadway powered electric vehicles," *IEEE Trans. Ind. Electron.*, vol. 63, no. 10, pp. 6533-6545, Oct. 2016.

[2] X. Liu, and S.Y. Hui, "Simulation study and experimental verification of a universal contactless battery charging platform with localized charging features," *IEEE Trans. Power Electron.*, vol. 22, no. 6, pp. 2202-2210, Nov. 2007.

[3] Q. Chen, S. C. Wong, C. K. Tse and X. Ruan, "Analysis, design, and control of a transcutaneous power regulator for artificial hearts," *IEEE Trans. Biomed. Circuits and Syst.*, vol. 3, no. 1, pp. 23-31, Feb. 2009.

[4] Y. Yang, W. X. Zhong, S. Kiratipoonvoot, S. C. Tan, and S. Y. R. Hui, "Dynamic improvement of series-series compensated wireless power transfer systems," *IEEE Trans. Power Electron.*, vol. 33, no. 7, pp. 6351-6360, Jul. 2018.

[5] M. Kim, D. Joo, and B. K. Lee, "Design and control of inductive power transfer system for electric vehicles considering wide variation of output voltage and coupling coefficient," *IEEE Trans. Power Electron.*, vol. 34, no. 2, pp. 1197-1208, Feb. 2019.

[6] Y. Yang, S. C. Tan, and S. Y. R. Hui, "Communication-free control scheme for Qi-compliant wireless power transfer system," in *Energy Conversion Congress and Exposition (ECCE)*, Sept. 2019, pp. 4955-4960.

[7] W. Zhang, S. C. Wong, C. K. Tse and Q. Chen, "Analysis and comparison of secondary series- and parallel-compensated inductive power transfer systems operating for optimal efficiency and load-independent voltage-transfer ratio," *IEEE Trans. Power Electron.*, vol. 29, no. 6, pp. 2979-2990, Jun. 2014.

[8] J. Yin, D. Lin, C. K. Lee, and S. Y. R. Hui, "A systematic approach for load monitoring and power control in wireless power transfer systems without any direct output measurement," *IEEE Trans. Power Electron.*, vol. 30, no. 3, pp. 1657-1667, Mar. 2015.

[9] J. Yin, D. Lin, C. K. Lee, and S. Y. R. Hui, "A systematic approach for load monitoring and power control in wireless power transfer systems without any direct output measurement," *IEEE Trans. Power Electron.*, vol. 30, no. 3, pp. 1657-1667, Mar. 2015.

[10] J. Yin, D. Lin, C. K. Lee, T. Parisini, and S. Y. R. Hui, "Front-end monitoring of multiple loads in wireless power transfer systems without wireless communication systems," *IEEE Trans. Power Electron.*, vol. 31, no. 3, pp. 2510-2517, Mar. 2016.

[11] J. Yin, D. Lin, T. Parisini, and S. Y. R. Hui, "Front-end monitoring of the mutual inductance and load resistance in a series-series compensated wireless power transfer system," *IEEE Trans. Power Electron.*, vol. 31, no. 3, pp. 7339-7352, Oct. 2016.

[12] Y. Yang, Y. Jiang, S. C. Tan, and S. Y. R. Hui, "A freqeuncy-sweep based load monitoring method for weakly-coupled series-series compensated wireless power transfer systems," in *IEEE PELS Workshop on Emerging Technologies: Wireless Power Trasnfer (WoW)*, Jun. 2018, pp. 1-5.

[13] K. Aditya and S. S. Williamson, "Design guidelines to avoid bifurcation in a series–series compensated inductive power transfer system," *IEEE Trans. Ind. Electron.*, vol. 66, no. 5, pp. 3973-3982, May 2019.

[14] Y. Yang, S. C. Tan, and S. Y. R. Hui, "Front-end parameter monitoring method based on two-layer adaptive differential evolution for SS-compensated wireless power transfer systems," *IEEE Trans. Ind. Informat.*, vol. 15, no. 11, pp. 6101-6113, Nov. 2019.

[15] Y. Yang, S. C. Tan, and S. Y. R. Hui, "Fast hardware approach to determining mutual coupling of series-series-compensated wireless power transfer systems with active rectifiers," *IEEE Trans. Power Electron.*, vol. 35, no. 10, pp. 11026-11038, Oct. 2020.

Front-End Voltage Regulations of Inductive Power Transfer Systems with Switched LCL Compensators

Kwing Hei Lo[1], Yun Yang[2], Ka-wai Eric Cheng[3]

1. Department of Electrical Engineering, The Hong Kong Polytechnic University, Hong Kong, kwinghei.lo@connect.polyu.hk.
2. Department of Electrical Engineering, The Hong Kong Polytechnic University, Hong Kong, yun1989.yang@polyu.edu.hk.
3. Department of Electrical Engineering, The Hong Kong Polytechnic University, Hong Kong, eric-cheng.cheng@polyu.edu.hk.

Abstract–In conventional inductive power transfer (IPT) systems, the output voltages are regulated by either the user-end DC regulators or the front-end inverters via wireless communications. However, the bulky sizes of the DC regulators and the communication devices may deteriorate the power densities of the receivers. To this end, a communication-free voltage regulation scheme is proposed for an LCL-S compensated IPT system by controlling the switched LCL compensator at the primary side. By measuring the front-end AC current of the transmitter resonator at the nominal condition, the output voltage of the IPT system can be estimated without any communication feedbacks. Based on the estimated output voltage, the primary-side controller can automatically switch on the desired compensated inductors, such that the output voltage can track the reference. The proposed scheme is validated by the simulation results in PSIM9.0.

Keywords–Inductive power transfer (IPT), LCL-S compensation, communication-free

I. INTRODUCTION

The electric vehicle (EV) industry has provided a wide range of possibilities for the future transportation [1]–[8]. This occurrence has led researchers to investigate this technology, such as the Wireless Power Transfer (WPT) systems, especially to the Inductive Power Transfer (IPT) systems [3]–[8]. Nonetheless, the EV sector is not the only one focused on this particular technology of the IPT technology [9]–[11]: wearables, medicines, applications where the possibility to introduce the human hand is not available, etc. It is due primarily to overly advantage of the total isolation between the primary/transmitter (typically a full-bridge controlled inverter) from the secondary/receiver (typically a full bridge diode rectifier). This fact makes this technology an excellent option for the future of the battery charger systems when the separation between the power source and the load is a priority.

The output voltage regulations of practical IPT systems are implemented by user-end DC regulators or the front-end inverters with the output feedback signals via wireless communications [12]–[18]. A schematic diagram of using a user-end DC regulator to control the output voltage of an IPT systems is shown in Fig. 1(a). Obviously, the existence of the DC regulator will increase the receiver size and may require additional power supply for the DC regulator. A schematic diagram of using a wireless communication device to feedback output voltage to the front-end inverter is shown in Fig. 1(b). The wireless communication devices will not only enhance the volume of both the transmitter and the receiver, but also brings additional high cost. Therefore, it is necessary to develop a cost-effective scheme to regulate output voltages of IPT systems without using DC regulators and wireless communication devices.
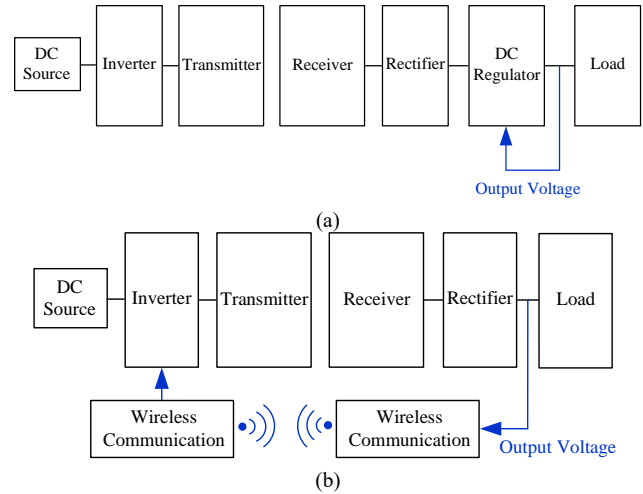

Fig. 1: Timing diagrams of the gate signals for the inverter.

This paper bridges the research gap by introducing a new switched LCL-compensation scheme at the front-end to regulate the output voltage without any communication between the transmitter and the receiver. The LCL-S compensation gains the merits of (i) null reflected reactance, (ii) continuous or discontinuous current operation, (iii) high efficiency at low-quality factor, (iv) variable frequency control to close to unity power factor, and (v) elimination of VAR loading for high power applications, as compared to the four basic compensation schemes, i.e., series-series (SS), series-parallel (SP), parallel-series (PS), and parallel-parallel (PP) compensation schemes [19]. Inherited from the conventional LCL-S compensation scheme, the proposed switched LCL-S compensation scheme possesses these aforementioned advantages, whereas extends the controllability by changing the fixed compensated inductor at the primary side to switched compensated inductors in multiple strings. The combinations of these inductor strings render the equivalent impedance of the IPT system alters, such that the output voltage can be regulated.

This paper is organized as following: (1) in Section II, the conventional LCL-S compensated IPT systems is briefly reviewed; (2) in Section III, the IPT system with the proposed switched LCL-S compensator is analyzed; (3) in Section IV, simulation results are exhibited to validate the effectiveness of the proposed scheme to regulate the output voltage of the IPT system; and (4) in Section V, conclusions are drawn.

II. A BRIEF REVIEW OF THE CONVENTIONAL LCL-S COMPENSATED IPT SYSTEMS

The circuit diagram of a typical LCL-S compensated IPT system is shown in Fig. 2. Here, both the compensated capacitors (i.e., C_p and C_s) are in resonances with the coil inductances (i.e., L_p and L_s), respectively, as
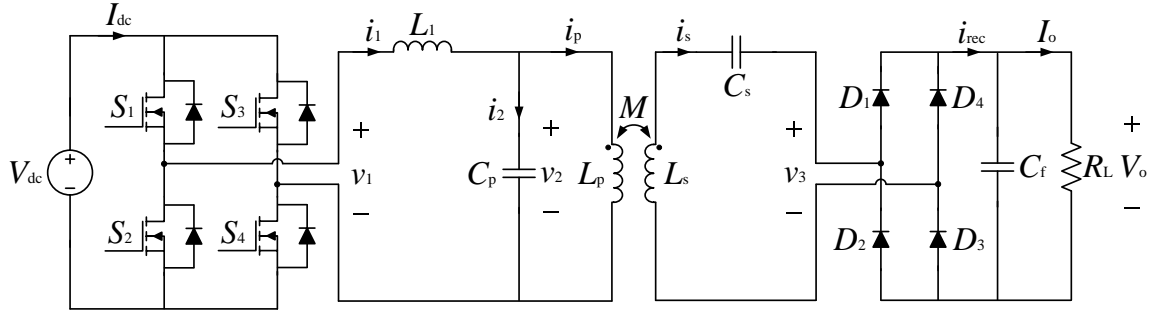
Fig. 2. Circuit diagram of a typical LCL-S compensated IPT system.

$$\omega^2 = \frac{1}{L_pC_p} = \frac{1}{L_sC_s} \tag{1}$$

where ω is the switching angular frequency of the IPT system. The compensated inductance L_1 equals to the self-inductance of the primary coil (i.e., $L_1 = L_p$). The switching signals S_1 and S_2, S_3 and S_4 are controlled to be complimentary and the switching signals S_1 and S_4, S_2 and S_3 are in phase. The timing diagrams of the four gate signals are depicted in Fig. 3.
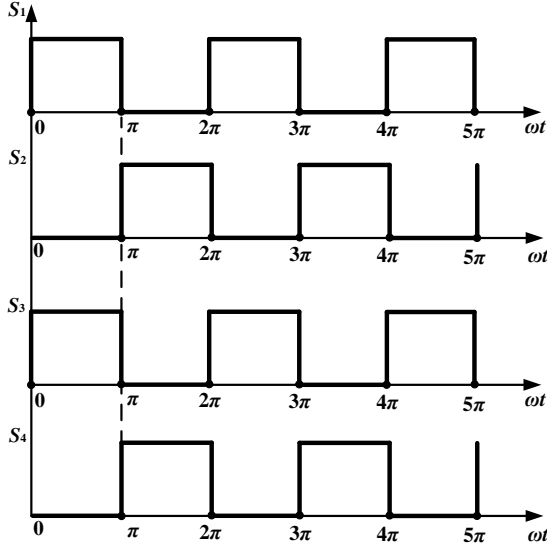

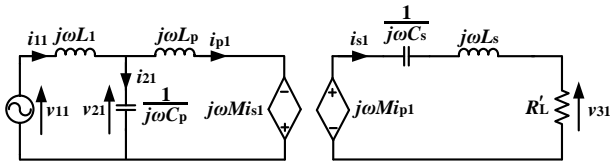Fig. 3: Timing diagrams of the gate signals for the inverter.

Fig. 4. Equivalent circuit of the conventional LCL-S compensated IPT system.

Based on the circuit diagram in Fig. 2, an equivalent circuit of the conventional LCL-S compensated IPT system can be depicted, as shown in Fig. 4. Here, the parameters v_{11}, i_{11}, i_{21}, v_{21}, i_{p1}, i_{s1}, and v_{31} are the fundamental components of v_1, i_1, i_2, v_2, i_p, i_s, and v_3, respectively. According to the Fourier analysis, the peak values of the v_{11}, i_{11}, v_{31}, and i_{s1}, i.e., V_{11}, I_{11}, V_{31}, and I_{s1} satisfy

$$V_{11} = \frac{4}{\pi}V_{dc} \tag{2.1}$$

$$I_{11} = \frac{\pi}{2}I_{dc} \tag{2.2}$$

$$V_{31} = \frac{4}{\pi}V_o \tag{2.3}$$

$$I_{s1} = \frac{\pi}{2}I_o \tag{2.4}$$

Besides, the equivalent load resistance R_L' satisfies

$$R_L' = \frac{8}{\pi^2}R_L \tag{2.5}$$

Based on the equivalent circuit and the Kirchhoff's laws,

$$v_{11} = j\omega L_1 i_{11} + \left(i_{11} - i_{p1}\right)\frac{1}{j\omega C_p} \tag{3.1}$$

$$j\omega M i_{p1} = \left(j\omega L_s + \frac{1}{j\omega C_s} + R_L'\right)i_{s1} \tag{3.2}$$

Due to the compensated inductance L_1 is designed to equalize the primary coil (i.e., $L_1 = L_p$), by substituting (1) into (3.1) and (3.2), respectively,

$$v_{11} = -\frac{i_{p1}}{j\omega C_p} \tag{4.1}$$

$$j\omega M i_{p1} = R_L' i_{s1} \tag{4.2}$$

By substituting (4.1) into (4.2) to eliminate i_{p1},

$$i_{s1} = \frac{M}{L_p R_L'} v_{11} \tag{5.1}$$

and

$$v_{31} = \frac{M}{L_p} v_{11} \tag{5.2}$$

Based on (5.1) and (5.2), the amplitudes of the parameters hold

$$I_{s1} = \frac{M}{L_p R_L'} V_{11} \tag{6.1}$$

$$V_{31} = \frac{M}{L_p} V_{11} \tag{6.2}$$

By substituting (2.1), (2.3), (2.4) and (2.5) into (6.1) and (6.2),

$$I_o = \frac{M}{L_p R_L} V_{dc} \tag{7.1}$$

$$V_o = \frac{M}{L_p} V_{dc} \tag{7.2}$$

Apparently, the output voltage of the conventional LCL-S compensated IPT system are dependent on the self-inductance of the primary coil (i.e., L_p), mutual inductance between the primary and secondary coils (i.e., M), and the input DC voltage (i.e., V_{dc}). The output current of the conventional LCL-S compensated IPT system also depends on the load resistance (i.e., R_L).

III. IPT Systems with the Proposed Switched LCL-S Compensators

By changing the fixed compensated inductor L_1 in Fig. 2 to switched compensated inductors (as shown in Fig. 5), the equivalent impedance of the IPT system can be regulated by controlling the switches in series with the compensated inductors (i.e., S_{L1}, S_{L2},…,S_{Ln}). By assuming the switched compensated inductors as an equivalent compensated inductor L_x, an equivalent circuit of the IPT system with the switched LCL-S compensator can be plotted, as shown in Fig. 6.

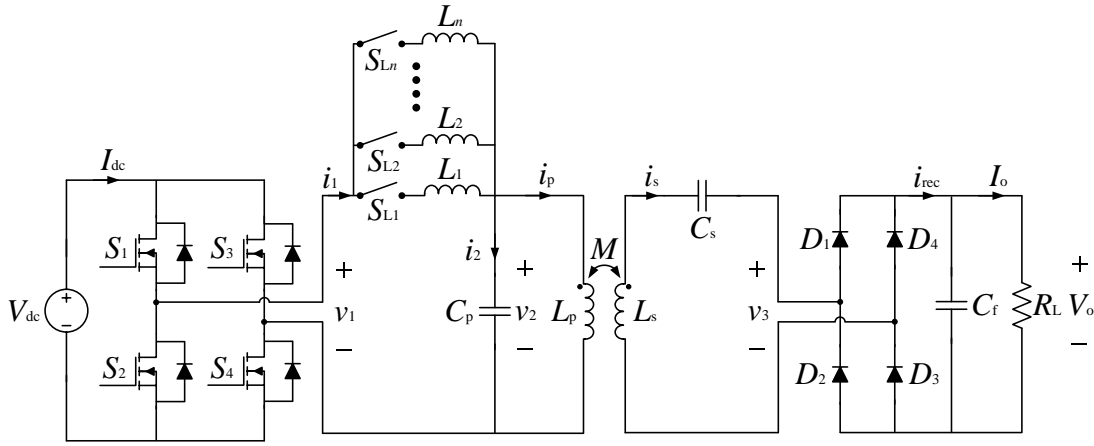Authors *et al*: Guidelines for Preparation of a Paper

Fig. 5. Circuit diagram of the IPT system with the proposed switched LCL-S compensator.
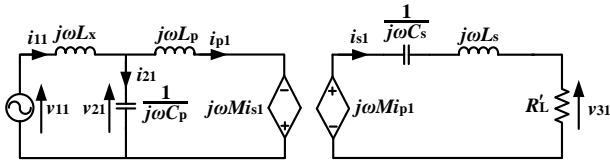

Fig. 6. Equivalent circuit of the IPT system with the switched LCL-S compensator.

Based on the equivalent circuit and the Kirchhoff's laws,

$$v_{11} = j\omega L_x i_{11} + (i_{11} - i_{p1})\frac{1}{j\omega C_p} \quad (8.1)$$

$$(i_{11} - i_{p1})\frac{1}{j\omega C_p} = j\omega L_p i_{p1} - j\omega M i_{s1} \quad (8.2)$$

$$j\omega M i_{p1} = \left(j\omega L_s + \frac{1}{j\omega C_s} + R_L'\right) i_{s1} \quad (8.3)$$

By substituting (8.2) and (8.3) into (8.1) to eliminate i_{11} and i_{p1},

$$i_{s1} = \frac{1}{\frac{8L_p R_L}{\pi^2 M} + \omega M\left(\frac{L_x}{L_p}-1\right)j} v_{11} \quad (9.1)$$

$$v_{31} = \frac{1}{\frac{L_p}{M} + \frac{\pi^2 \omega M}{8R_L}\left(\frac{L_x}{L_p}-1\right)j} v_{11} \quad (9.2)$$

Based on (5.1) and (5.2), the amplitudes of the parameters hold

$$I_{s1} = \frac{1}{\sqrt{\left(\frac{8L_p R_L}{\pi^2 M}\right)^2 + \omega^2 M^2\left(\frac{L_x}{L_p}-1\right)^2}} V_{11} \quad (10.1)$$

$$V_{31} = \frac{1}{\sqrt{\left(\frac{L_p}{M}\right)^2 + \left(\frac{\pi^2 \omega M}{8R_L}\right)^2\left(\frac{L_x}{L_p}-1\right)^2}} V_{11} \quad (10.2)$$

By substituting (2.1), (2.3), (2.4) and (2.5) into (10.1) and (10.2),

$$I_o = \frac{\frac{8}{\pi^2}}{\sqrt{\left(\frac{8L_p R_L}{\pi^2 M}\right)^2 + \omega^2 M^2\left(\frac{L_x}{L_p}-1\right)^2}} V_{dc} \quad (11.1)$$

$$V_o = \frac{1}{\sqrt{\left(\frac{L_p}{M}\right)^2 + \left(\frac{\pi^2 \omega M}{8R_L}\right)^2\left(\frac{L_x}{L_p}-1\right)^2}} V_{dc} \quad (11.2)$$

By taking partial derivative of V_o over L_x in (11.2),

$$\frac{\partial V_o}{\partial L_x} = \frac{\frac{V_{dc}}{L_p^2}\left(\frac{\pi^2 \omega M}{8R_L}\right)^2 (L_p - L_x)}{\left[\left(\frac{L_p}{M}\right)^2 + \left(\frac{\pi^2 \omega M}{8R_L}\right)^2\left(\frac{L_x}{L_p}-1\right)^2\right]^{\frac{3}{2}}} \quad (12)$$

Based on the derivations in (11.2) and (12), a plot of V_o versus L_x can be depicted as shown in Fig. 7. The maximum output voltage (i.e., $V_{omax} = \frac{M}{L_p}V_{dc}$) can be achieved by controlling the equivalent compensated inductance

equaling the inductance of the primary coil (i.e., $L_x = L_p$). When the output voltage is required to be less than the maximum output voltage, the equivalent compensated inductance is controlled based on (11.2) by switching on proper inductor strings. The mutual inductance and the load resistance can be preliminarily measured or estimated using the identification methods in [17].
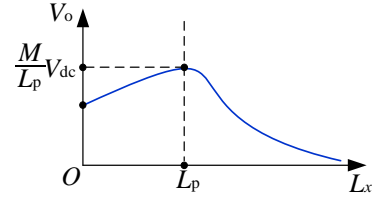
Fig. 7. Plot of V_o versus L_x for the IPT system.

IV. SIMULATION RESULTS

Simulations are carried out in PSIM 9.0. The parameters of the IPT system are listed in Table 1. Initially, the conventional LCL-S compensation is adopted, whereas the compensated inductance (i.e., L_x) is changed with different parameters. The simulated curves of the output voltage (i.e., V_o) versus the compensated inductance (i.e., L_x) for different load and mutual inductance conditions are plotted in Fig. 8. Apparently, the simulated curves are similar to the analytical curve in Fig. 7.

Table 1: Specifications of the IPT system in simulation

Parameter	Symbol	Value
Nominal frequency	f_0	100 kHz
DC voltage source	V_{dc}	21 V
Transmitter coil inductance	L_p	49.2 μH
Receiver coil inductance	L_s	49.2 μH
Transmitter compensated capacitance	C_p	51.484 nF
Receiver compensated capacitance	C_s	51.484 nF
Filter capacitance	C_f	100 μF
Nominal load resistance	R_L	1 Ω
Nominal mutual inductance	M	9.84 μH

Authors *et al*: Guidelines for Preparation of a Paper

(a) nominal mutual inductance and nominal load resistance

(b) nominal mutual inductance and R_L=0.5 Ω

(c) nominal mutual inductance and R_L=2 Ω

(d) M=14.76 μH and nominal load resistance

(e) M=24.6 μH and nominal load resistance
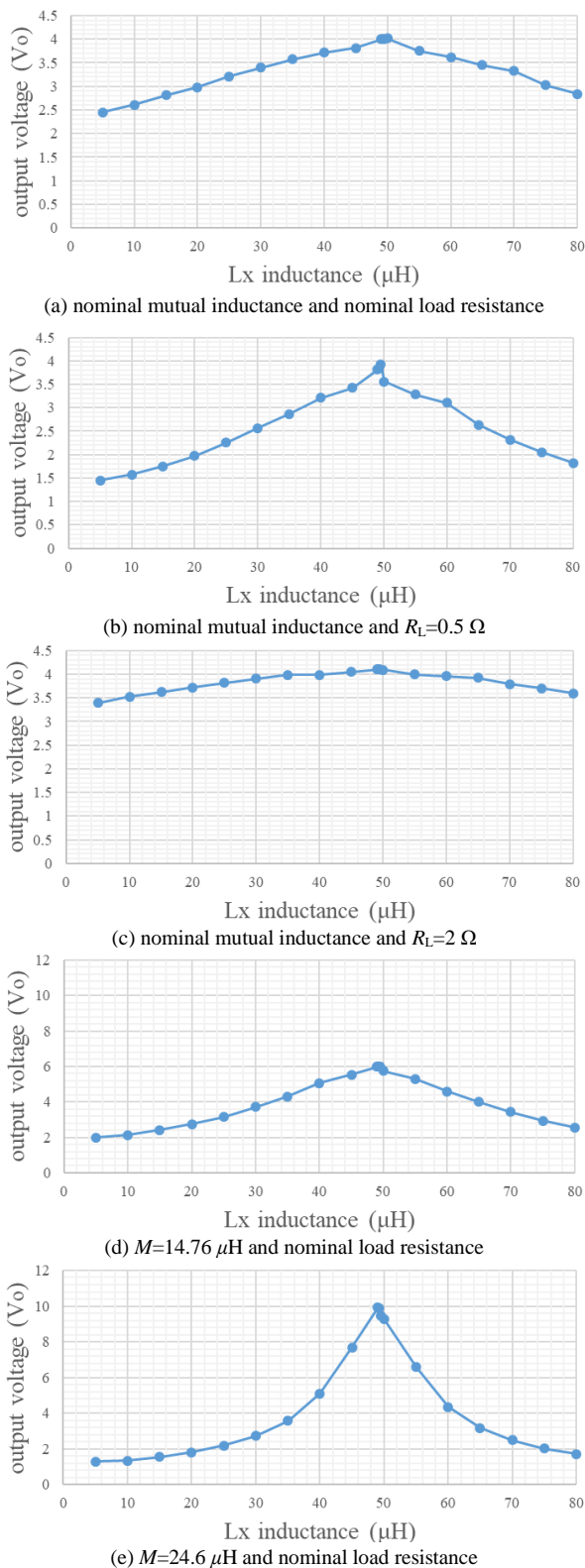
Fig. 8. Simulated curves of V_o versus L_x for different load and mutual inductance conditions.
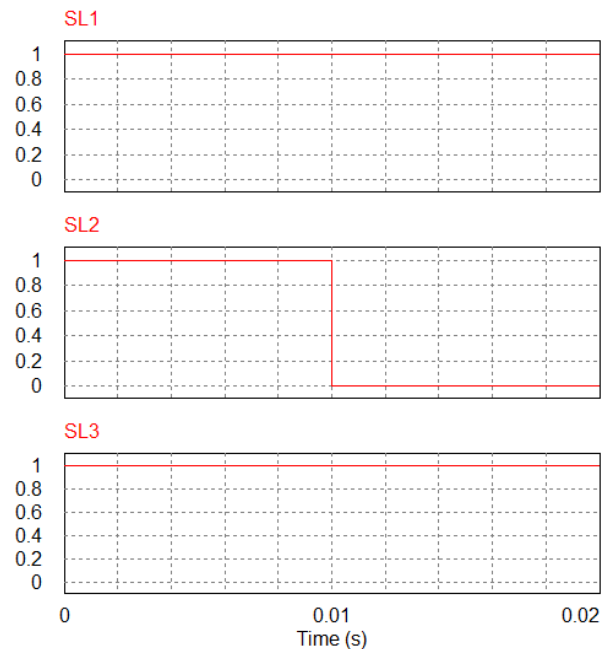
Then, a switched compensator with three compensated inductor strings are adopted. The inductances of the three strings are L_1=38 μH, L_2=46 μH and L_3=1.2 mH, respectively. By controlling the switches S_{L1}, S_{L2} and S_{L3}, the output voltage of the IPT system with the proposed switched LCL-S compensator can be regulated. Three cases with different mutual inductances and load conditions are investigated, as provided in Table 2. In case 1, both the mutual inductance and load condition are nominal. The output voltage reference is changed from 3 V to 3.5 V. In

case 2, the mutual inductance is nominal, whereas the load resistance is 0.5 Ω. The output voltage reference is changed from 3 V to 2 V. In case 3, the load condition is nominal while the mutual inductance is 24.6 μH. The output voltage reference is changed from 4 V to 8 V.

Table 2: Case studies of the IPT system with three compensated inductor strings

Case number	Mutual inductance (μH)	Load resistance (Ω)	Output voltage reference (V)
1	9.84	1 Ω	3 V→ 3.5 V
2	9.84	0.5 Ω	3 V→ 2 V
3	24.6	1 Ω	4 V→ 8 V

Fig. 9 show the waveforms of the switching signals S_{L1}, S_{L2} and S_{L3} and the corresponding output voltages of the IPT system in the three cases. In case 1, all the switches S_{L1}, S_{L2} and S_{L3} are ON at the beginning. At the time t=0.01 s, the switch S_{L2} is turned OFF while the switches S_{L1} and S_{L3} are still ON. Accordingly, the output voltage is changed from 3 V to 3.53 V. Obviously, the output voltage is well-regulated to the reference. The corresponding currents of i_1, i_{Lp}, and i_{Ls} are shown in Fig. 9(a). In case 2 (as shown in Fig. 9(b)), the switch S_{L1} is ON while the switches S_{L2} and S_{L3} are OFF initially. At the time t=0.01 s, all the three switches are ON. Accordingly, the output voltage is changed from 2.954 V to 1.995 V. Apparently, the output voltage is also well-regulated to track the reference in case 2. Similarly, in case 3 (as shown in Fig. 9(c)), the output voltage is controlled from 3.97 V to 8.02 V, which tracks the reference accurately.

Authors *et a*l: Guidelines for Preparation of a Paper
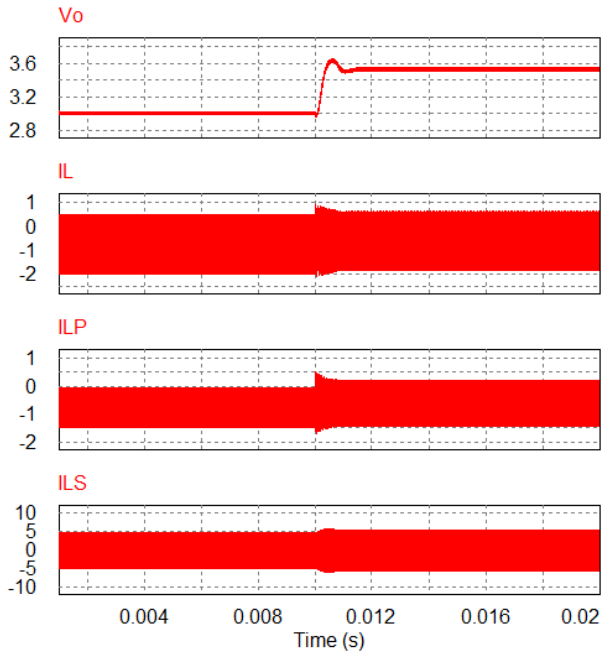
(a) case 1
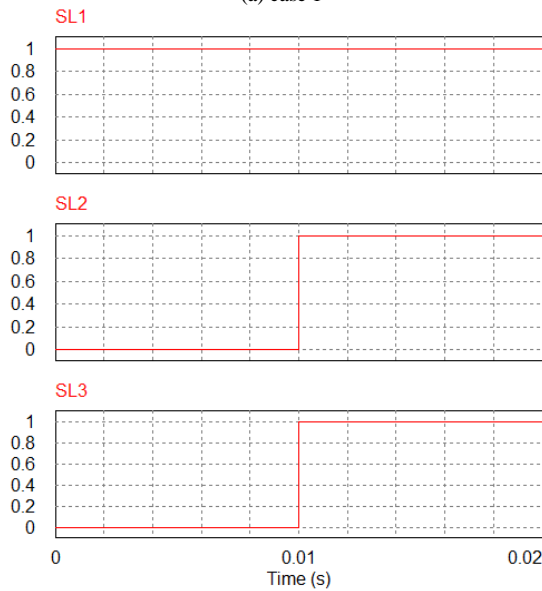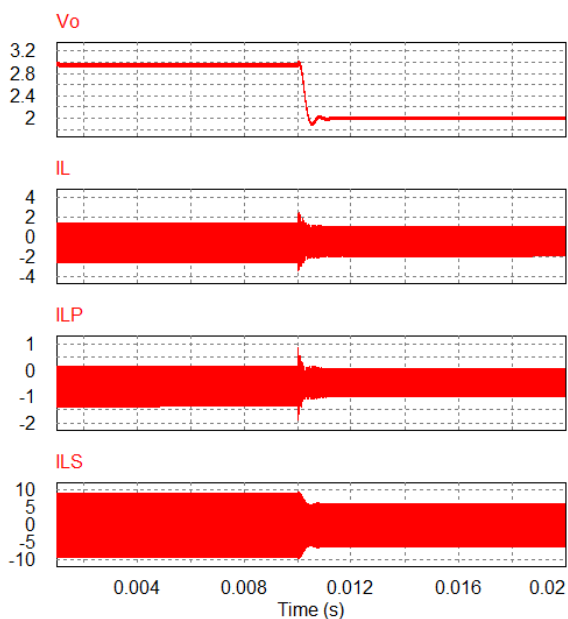
(b) case 2
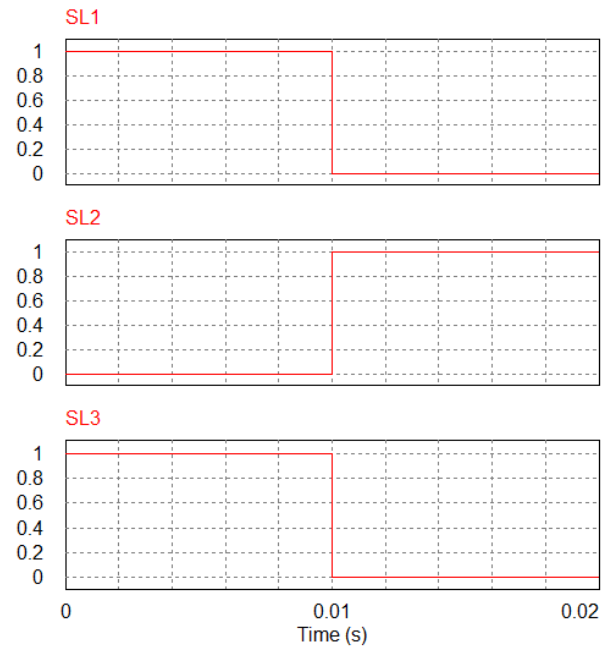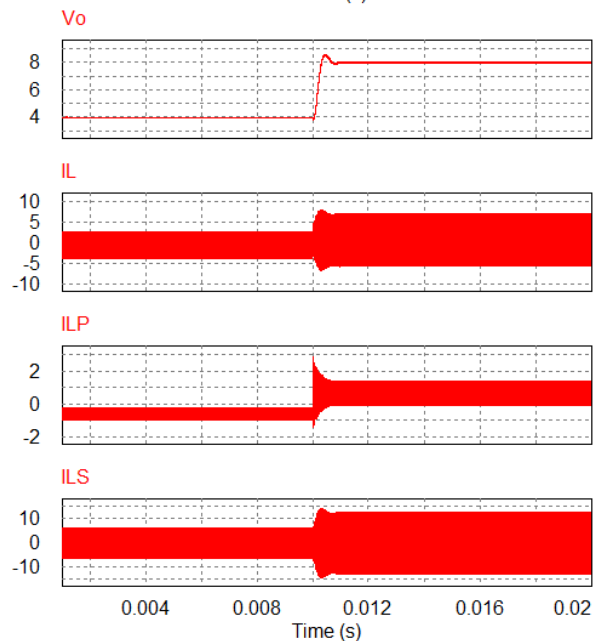
(c) case 3

Fig. 9. Simulated waveforms of the switching signals and the output voltages of the IPT system with the three compensated inductor strings.

V. CONCLUSION

In this paper, switched compensated inductor strings are proposed to substitute the fixed compensated inductor of the classic LCL-S compensation for IPT systems to regulate the output voltages at the front-end without using wireless communications between the transmitters and the receivers. The proposed scheme can improve the power densities of the receivers of the IPT systems by eliminating the bulky DC regulators and communication devices. Simulation results have verified the analysis of the relationships between the output voltages and the compensated inductances. The output voltages are also validated to track the references accurately in different mutual inductance and load conditions.

REFERENCES

[1]   C. Chan, K. Chau, et al., *Modern electric vehicle technology*, no. 47, Oxford University Press on Demand, 2001.

[2] C. D. Xu and K. W. E. Cheng, "All-electric intelligence anti-lock braking controller for electric vehicle under complex road condition," in *Int. Symp. Electr. Eng. (ISEE)*, Dec. 2016, 1-5.

[3] G. Covic and J. T. Boys, "Inductive power transfer," *Proc. of IEEE*, vol. 101, no. 6, pp. 1276-1289, Jun. 2013.

[4] A. W. Green and J. T. Boys, "10 kHz inductively coupled power transfer-concept and control," in *Proc. 5th Int. Conf. Power Electron. Variable-Speed Drives*, 1994, pp. 694-699.

[5] G. A. J. Elliott, J. T. Boys, and A. W. Green, "Magnetically coupled systems for power transfer to electric vehicles," in *Proc. Int. Conf. Power Electron. Drives Syst.*, 1995, vol. 2, pp. 797-801.

[6] J. R. Severns, E. Yeow, G. Woody, J. Hall, and J. Hayes, "An ultra-compact transformer for a 100 W to 120 kW inductive coupler for electric vehicle battery charging," in *Proc. 11th Annu. IEEE Appl. Power Electron. Conf. Expo.*, 1996, vol. 1, pp. 32-38.

[7] J. T. Boys, G. A. Covic, and A. W. Green, "Stability and control of inductively coupled power transfer systems," *Inst. Electr. Eng. Proc.—Electr. Power Appl.*, vol. 147, no. 1, pp. 37-43, 2000.

[8] J. T. Boys, G. A. J. Elliott, and A. W. Green, "An appropriate magnetic coupling co-efficient for the design and comparison of ICPT pickups," *IEEE Trans. Power Electron.*, vol. 22, no. 1, pp. 333-335, Jan. 2007.

[9] P. Si, A. P. Hu, S. Malpas, and D. Budgett, "A frequency control method for regulating wireless power to implantable devices," *IEEE Trans. on Bio. Circuits and Syst.*, vol. 2, pp. 22–29, Mar. 2008.

[10] X. Li, C. Tsui, and W. Ki, "A 13.56 MHz wireless power transfer system with reconfigurable resonant regulating rectifier and wireless power control for implantable medical devices," *IEEE J. of Solid- State Circuits*, vol. 50, pp. 978–989, Apr. 2015.

[11] U. Jow and M. Ghovanloo, "Design and optimization of printed spiral coils for efficient transcutaneous inductive power transmission," *IEEE Trans. on Bio. Circuits and Syst.*, vol. 1, pp. 193–202, Sept. 2007.

[12] Y. Yang, W. X. Zhong, S. Kiratipoonvoot, S. C. Tan, and S. Y. R. Hui, "Dynamic improvement of series-series compensated wireless power transfer systems," *IEEE Trans. Power Electron.*, vol. 33, no. 7, pp. 6351-6360, Jul. 2018.

[13] Y. Yang, S. C. Tan, and S. Y. R. Hui, "Communication-free control scheme for Qi-compliant wireless power transfer system," in *Energy Conversion Congress and Exposition (ECCE)*, Sept. 2019, pp. 4955-4960.

[14] W. Zhang, S. C. Wong, C. K. Tse and Q. Chen, "Analysis and comparison of secondary series- and parallel-compensated inductive power transfer systems operating for optimal efficiency and load-independent voltage-transfer ratio," *IEEE Trans. Power Electron.*, vol. 29, no. 6, pp. 2979-2990, Jun. 2014.

[15] Y. Yang, Y. Jiang, S. C. Tan, and S. Y. R. Hui, "A freqeuncy-sweep based load monitoring method for weakly-coupled series-series compensated wireless power transfer systems," in *IEEE PELS Workshop on Emerging Technologies: Wireless Power Trasnfer (WoW)*, Jun. 2018, pp. 1-5.

[16] K. Aditya and S. S. Williamson, "Design guidelines to avoid bifurcation in a series–series compensated inductive power transfer system," *IEEE Trans. Ind. Electron.*, vol. 66, no. 5, pp. 3973-3982, May 2019.

[17] Y. Yang, S. C. Tan, and S. Y. R. Hui, "Front-end parameter monitoring method based on two-layer adaptive differential evolution for SS-compensated wireless power transfer systems," *IEEE Trans. Ind. Informat.*, vol. 15, no. 11, pp. 6101-6113, Nov. 2019.

[18] Y. Yang, S. C. Tan, and S. Y. R. Hui, "Fast hardware approach to determining mutual coupling of series-series-compensated wireless power transfer systems with active rectifiers," *IEEE Trans. Power Electron.*, vol. 35, no. 10, pp. 11026-11038, Oct. 2020.

[19] C. Jiang, K. T. Chau, C. Liu, and C. H. T. Lee, "An overview of resonant circuits for wireless power transfer," *Energies*, vol. 10, no. 7, pp. 894, Jun. 2017.

Planar Printed-Circuit-Board (PCB) Transformers with Active Clamp Flyback Converter for Low Power AC-DC Adapter Application

Y.L. Ho[1], K.W.E.Cheng[2], Kin Lung Jerry Kan[3], H.S.Chung[4], Wan Yee Lam[5]

Power Electronics Research Centre, Department of Electrical Engineering

The Hong Kong Polytechnic University, Hong Kong

E-mail: yl2018ho@polyu.edu.hk   eeecheng@polyu.edu.hk   jerry.kan@connect.polyu.hk

Abstract—With ever-increasing demands of smaller size, lighter weight for all forms of AC-DC consumer electronics, and wire winding transformers have been most used in isolated adaptor for over a century. The most popular isolated AC-DC adaptor topology is the flyback, but the leakage inductance and switching losses of a traditional flyback limit the switching frequency and prevent the ability to achieve a small solution size. This paper demonstrates new ways to optimize flyback topology with planar PCB-embedded transformer to produce much higher efficiencies, even while switching at a higher frequency for adapter application.

Keywords: Energy storage, Electric Vehicles, Redox flow battery, super-capacitor, fuel cell, active suspension, in-wheel motor, configurable EV, ABS.

I. INTRODUCTION

Power converter design is a major industry in the power conversion market [1-8]. In particular, the AC/DC power converter that is being used substantially for traveling and Power delivery (PD) is now a hot topic. It is expected that the market share is very large and is over $9 Billion in 2019. The users include smartphones, tablets, and a number of the mobile electronic appliance. The cost and size are the main driving force for the new generation of development. The operation frequency is usually limited to 100kHz because of the conservation design of switching loss at high frequency.

This paper targets 65W adaptor applications. With the resonant power technique and the switching loss can be reduced and the hence the soft switching version of flyback converter circuit should be chosen because of simple and low cost.The isolated version of the buck-boost converter that is commonly known as flyback converter is the proper topology for AC-DC conversion because of the simple topology and low component count. For the non-soft-switching version, a snubber or RCD clamp circuit is usually used to suppress the loss and spike voltage due to the leakage components and the design limits its switching frequency to 100kHz. The active clamp flyback (ACF) converter can clamp and recycle the voltage of transformer leakage energy [1, 2, 3]. Active clamp flyback with synchronous rectifier (SR) circuit is shown in Fig. 1. Its structure is simple: Certain clamping circuit can generate the zero-voltage switching (ZVS) and its leakage energy can be recycled to the source. In general, there are two operation modes which is so called the Discontinuous Conduction Condition (DCC) and the Continuous Conduction Condition (CCC). The DCC with SR method works current resonant switching but because of the current resonance, its current is therefore with high amplitude and the auspicated loss is larger. On the other hand, the CCC operation with less current stress, but its voltage stress is high in the secondary SR. The design is used pre-off topology of SR control to fast turn off and reduced SR's reverse-recovery loss in CCC condition.

Transformers are major components used for electrical isolation and energy transfer with power supplies application. The transformer consists of copper winding and also the magnetic core. No matter it is machine wounded or handmade, the tolerance of the turns per layer, packaging factor, separation between the winding layers are different and hence the tolerance of different transformers may vary a lot. Quality assurance is the major benefit of the planar PCB-embedded transformer, because of eliminates the manual winding process. Unfortunately, the leakage inductance and parasitic capacitance of a planar PCB-embedded transformer limit the switching frequency and prevent the ability to achieve a small solution size [6, 7]. Fortunately, there are new ways to optimize the flyback

topology and transformer winding structure to produce much higher efficiencies, even while switching at a higher frequency with the AC adaptor application.

The working condition changes due to different input voltage in the universal application, challenging both exist switching devices tradeoff and transformer designs in AC-DC adaptor application. At low line input voltages, the on-stat loss of the primary switches components dominates due to the higher current. As the high line input voltage, the switching loss of the primary switches components due to higher dv/dt [5]. As a result, theDCC and CCC mode selection is more difficult in the design. The magnetic component design including the winding method, coupling, and winding ratio are key design information. The current-mode PWM controller, HY1801 from HYSEMI, is a high-performance Active-Clamp Flyback controller that uses proprietary ZVS tracking technology. The HY1801 uses different operating modes to optimize the conversion efficiency under the various lines, including Active-Clamp Mode, 140kHz Constant Frequency Mode. The switching frequency of the Active clamp Flyback converter using HY1801 is optimized to operate up to 250kHz.

The active clamp resonance time can have a wide variation depending on the transformer leakage inductance, the clamping capacitor values, and other parasitic parameters. Although the HY1801 can track the ZVS automatically, it is still necessary for the application design to provide the resonance time information to allow the algorithm to operate more efficiently. To simplify the application, the operation schematics and resonance time thesis are used as shown in Fig. 2 & 3.
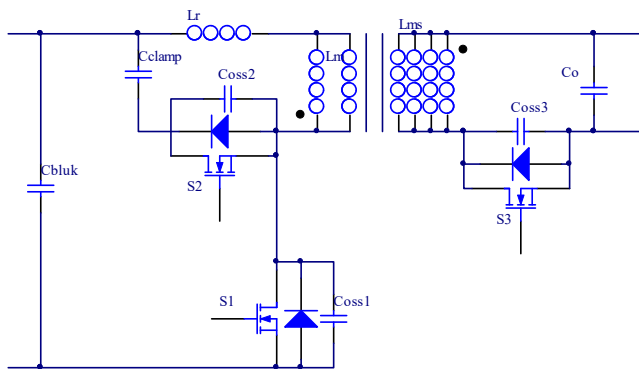
Fig.1 Active clamp flyback converter with syn. rectifier
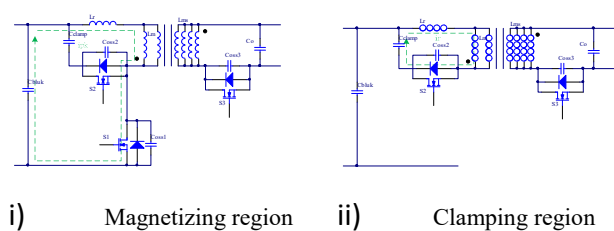
i)   Magnetizing region   ii)   Clamping region
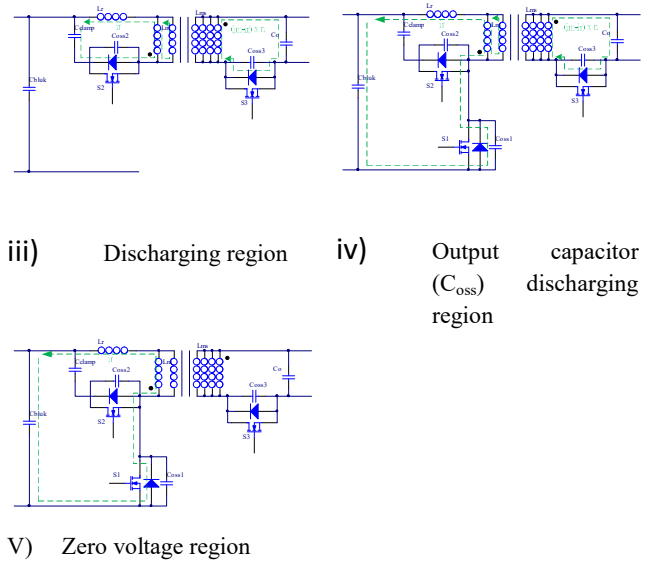
iii)   Discharging region   iv)   Output   capacitor (C_{oss}) discharging region

V)   Zero voltage region

Fig. 2 Active Clamp operation circuit diagram
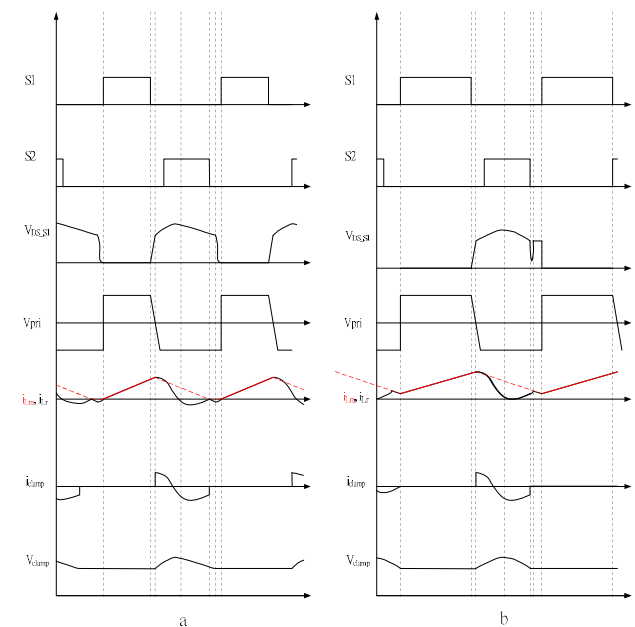
Fig. 3 Typical waveforms of ACF of (a) DCC, and (b) CCC

The characteristics between the DCC and CCC are different in terms of the control and ripple current. Researches may consider the DCC because of easy design and more linear control features, however, the ripple is large and therefore the filter capacitor may needs to increase.

II. METHODOLOGY

A. Circuit Operation and Turns Ratio study

Previous section has described the initial study of the ACF topology. It is simple and of high efficiency in high frequency operation to optimized size. Fig. 3 illustrates the key waveforms of DCC and CCC operation. In fact the magnetizing currentaffects and determines the operation in continuous and discontinuous mode. It is found that there is negative region of operation i_{Lm} in DCC whereas i_{Lm} is always positive when the operation is under CCC.The DCC condition is when the ΔI_{Lm} larger than 2 times of I'_{Lm}:

$$\Delta I_{Lm} \geq 2I'_{Lm} \qquad (1)$$

$$I'_{Lm} = \frac{Io}{n} \times \frac{Vin + nVo}{Vin} \qquad (2)$$

The design criterion is to focus on the reduction of the loss of the active components rather than the total loss reduction. Proper design of L_r and L_m to ensure which operation mode to work on and the associated turns ratio and frequency are determined. Because the maximum operating frequency of the ACF is up to 250kHz, it is more desired to DCC operation in the universal input voltage to safeguard operation. Thesimulation results are shown andthe typicalwaveform of the active clamp flyback circuit with different the input voltage V_{in} in optimized transformer parametersare illustrated in Fig. 6. It shows that the DCCis operated with ZVS until full loading condition in the universal input voltage.

B. Transformer Design and Optimization

Integration of the magnetic components to the PCB is proposed here. Hence the former for winding is eliminated. The magnetic components can be significantly reduced in size because the winding and the magnetic parts are highly integrated and the space between the original winding is eliminated. This is now called PCB-embedded transformer.

The core selection is referring to manufactory's core selection guide. The core suggested in table 1 is typical for universal input range, 67kHz switching frequency and single output application[9]. ATQ25 is selected for the 65W ACF universal adaptor application. Because of 65WACF adaptor is operation up to 250kHz, that is much higher than 67kHz, a small core can be selected.

Table 1 Core quick selection table

Output Power (W)	EI core	EE Core	ERR Core	EPC Core
0-10	EI12.5 EI16 EI19	EE8 EE10 EE13 EE16		EPC10 EPC13 EPC17
10-20	EI22	EE19		EPC19
20-30	EI125	EE22	EER25.5	EPC25
30-50	EI28 EI30	EE25	EER28	EPC30
50-70	EI35	EE30	EER28L	
70-100	EI40	EE35	EER35	
100-150	EI50	EE40	EER40 EER42	
150-200	EI60	EE50 EE60	EER49	

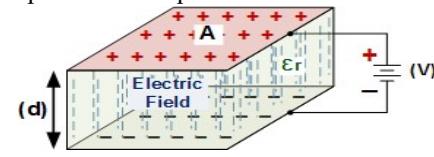(For universal input voltage range, fs = 67kHz and single output)

The transformer turn ratio (n) is depend on voltage of switching device and output voltage, the most comment used switching device of primary and secondary are 700V and 100V respectively.

$$V_{DS\_S1(max)} \times \text{Derating } \% \geq 1.1 \times \left[\sqrt{2}V_{in(max)} + n(V_o + V_{F)]}\right] \qquad 4)$$

$$V_{DS\_S3(max)} \times \text{Derating } \% \geq 1.1 \times \left[\frac{1}{n}\sqrt{2}V_{in(max)} + (V_o + V_{F)]}\right] \qquad (5)$$

The turns ratio of transformer is chosen 7 that between 6.25 and 7.5

Parasitic capacitance is major challenging of a planar PCB-embedded transformer limit the switching frequency. The 65W PCB-embedded transformer is used a different multilayer structure in the primary & secondary winding to optimize the capacitance.

$$C = \frac{\varepsilon \times A}{d} \qquad (6)$$

Because of secondary side is small number of turn, the parallel structure in 4 layers PCB with via to ensure equal potential to each layer. In the primary side, the interleaving and sandwich structure in series of 2 pieces 2 layers PCB to reduce the dielectric area (A) and increase electric distance (d). The PCB-embedded transformer structure and model circuit are shown as Fig. 4 and Fig. 5.
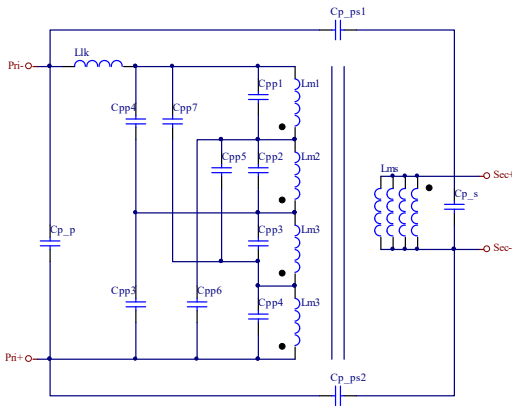
Fig. 4 Model circuit of high frequency PCB-embedded Transformer
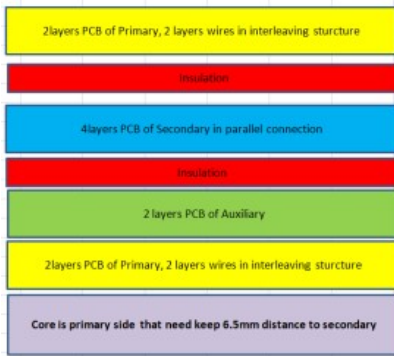
a) Transformer winding cross section
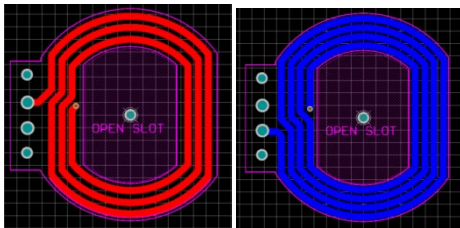
b) Primary winding PCB layout
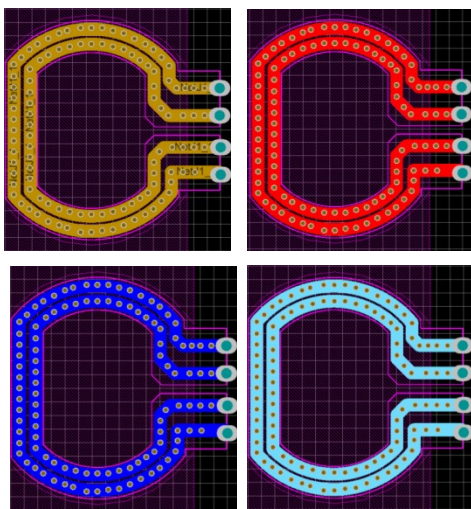
c) Secondary winding PCB layout

Fig. 5 Flyback transformer winding structure & PCB layout

III. SIMULATION AND RESULT

The Multi layer PCB-embedded transformer optimization is to maximize power density and operation frequency. There are four optimization factors: the primary track width, secondary track width, coupling area, coupling distanceand the power transfer turn number*n*. In the ATQ25 transformer core, the frequency response of PCB-embedded transformer is Fig. 6. It shows a typical characteristic. According the result, the 0.7mm track with interleaving can be used in HY1801 ACF application. The optimized parameters of PCB-embedded transformer are shown Table 2:

a)   0.6mm track interleaving   b) 0.7mm track interleaving

Fig. 6 Impedance Response of Transformer with difference interleaving levels

Table 2 Optimized parameters of PCB-embedded transformer

L_m	162 μH
L_{lk}	4.9 μH
Rs	0.55Ω
L_{ms}	4.07 μH
R_{ss}	0.105Ω

The selected parameters are reasonable for power conversion design parameter. They are all within the design range.

In order to study the performance further a simulation using PSpice based simulator has been conducted. The study is to examine the operation under different load conditions and its effect to its operation against the design criteria.
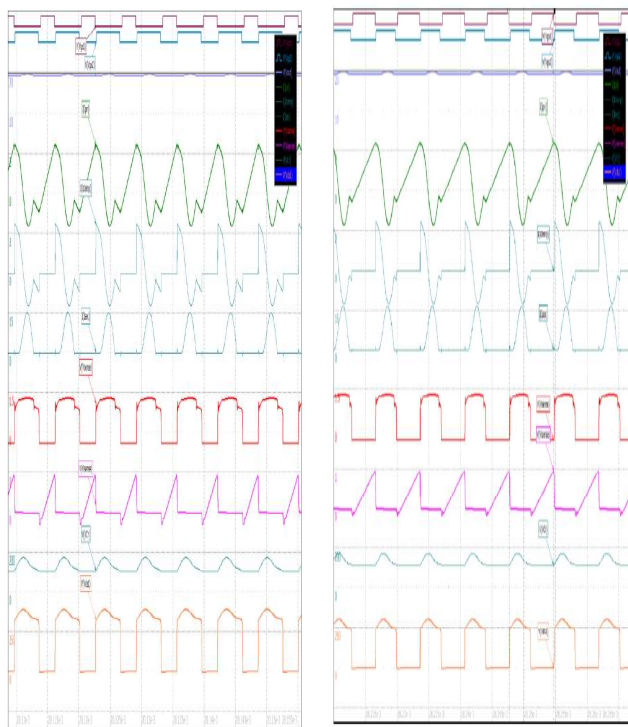
a) 110Vac 20V 3.25A   b) 230Vac 20V 3.25A
   loading   loading

Fig. 7 Simulation waveforms of universal input voltage ACF

Fig. 7 shows the simulation results in full load condition at universal input voltage. The output voltage, SR current, clamping current, clamping voltage, transformer current, drain-source voltage of the S1, gate signals of S_1 and S_2 are nomenclated as V_o, I_{sec}, I_{clamp}, V_{cr}, I_{pri}, V_{ds1}, V_{gs1}, and V_{gs2}, respectively.ZVS operation of switching devices are successes because the Mosfet's body diode conduct before devices turn on under universal input voltage.

VI. SUMMARY AND CONCLUSION

Leakage inductances and self-parasiticcapacitance of PCB-embedded planer magnetic device with various geometric factors have been examined. Based on an analytical method, the self-parasitic capacitance of PCB-embedded planer transformers can be controlled. The frequency response results have been confirmed with the impedance analysis measurements. The frequency response of PCB-embedded planer transformers depends on the interleaving area and conduct track width. Variations of interleaving area and conduct track width affect all of the capacitance parameters. The self-parasitic capacitance of planer PCB-embeddedtransformers is a proportion to track width and interleaving area. The frequency response of PCB-embedded planer transformer is affected by self-capacitance. The frequency characteristics of PCB-embedded planer transformer is measuredthe testing frequency ranges between 50 kHz to 500 kHz. It shows that the magnetize impedanceof the transformeragainst frequency do not changed significantly.

This paper examines the 65W ACF converter with a PCB-embedded planar transformer for the use in low power adaptors. The ACF topology is proposed because of its advantage in the tradeoff against simplicity, high power density and efficiency. SR topology is also selected for increasedefficiency to aid small size. The PCB-embedded technique improve significantly the power density. A simulation is conducted and it achieves a ZVS in a universal input range of 110 V to 230 V. Furthermore, the ACF adaptor prototype is under building.

REFERENCES

[1] C. T. Choi, C. K. Li, and S. K. Kok, "Control of an active clamp discontinuous conduction mode flyback converter," in *Proc. IEEE Power Electronics and Drive Systems Conf.*, 1999, vol. 2, pp. 1120- 1123.

[2] R. Watson, F. C. Lee, and G. Hua, "Utilization of an Active-Clamp Circuit to achieve Soft Switching in Flyback Converters," *IEEE Trans.on Power Electron., vol.11, pp162-169, January 1996.*

[3] J. Zhang, X. Huang, X. Wu, and Z. Qian, "A high efficiency flyback covnerter with new active clamp technique," *IEEE Trans.on Power Electron.*, vol.25, No. 7, pp1775-1785, Jul. 2010

[4] M. Mu, F. C. Lee, "A new core loss model for rectangular AC voltages," in proc. IEEE ECCE, 2014, pp 5214-5220. 2506-2508.

[5] Xiucheng Huang, Junjie Feng, Weijing Du, Fred C. Lee, and Qiang Li, "Design Consideration of MHz Active Clamp Flyback Converter with GaN Devices for Low Power Adapter Application" IEEEApplied Power Electronics Conference and Exposition (APEC). 2016

[6] S. C. Tang, S. Y. (Ron) Hui, and Henry Shu-Hung Chung," Coreless Planar Printed-Circuit-Board (PCB) Transformers—A Fundamental Concept for Signal and Energy Transfer" IEEE Transactions On Power Electronics, VOL. 15, NO. 5, September 2000

[7] S. C. Tang, S. Y. (Ron) Hui, and Henry Shu-Hung Chung," Characterization of Coreless Printed Circuit Board (PCB) Transformers" IEEE TRANSACTIONS ON POWER ELECTRONICS, VOL. 15, NO. 6, NOVEMBER 2000

[8] Reportlinker, "AC-DC Power Supply Adapter Market – Global Industry Analysis, Size, Share, Growth, Trends, and Forecast, 2019 – 2027" Report linker June 2020

[9] "Design Guidelines for Off-line Flyback Converters Using Fairchild Power Switch"On semiconductor application note AN4137 2003

100kW Electric Bus Wireless Charging System with Calculating Method for Hybrid Energy Storage Capacity

Wenzhou Lu[1*], Jian Zhao[1], Yifan Dong[1], Bo Wang[2], Jinfei Shen[1]

[1]School of Internet of Things Engineering, Key Laboratory of Advance Process Control for Light Industry (Ministry of Education), Jiangnan University, Wuxi 214122, China.

[2]School of Electrical Engineering, Southeast University, Nanjing 210096, China

E-mail: luwenzhou@126.com

Abstract – For the application background of electric buses being wirelessly charged at the stopping locations on bus route, a 100 kW electric bus wireless charging system with supercapacitor (SC)-battery hybrid energy storage is designed. In addition, a calculating method for hybrid energy storage capacity is proposed to select the appropriate capacities of system hybrid energy storage devices and thus reduce the weight of bus. Firstly, the equivalent circuit model of the wireless power transfer (WPT) system with SC and battery being loads is analyzed. Then, for the dynamic change of SC equivalent resistance, the SC detection, the wireless data communication, and the power regulation are adopted in the system. Finally, the 100 kW wireless charging system designed in this paper is implemented and verified by experiments. When the transfer distance is 0.45 m, the output power can be 80.2 kW with 89.6% transfer efficiency. Moreover, according to the experimental results and the bus energy consumption survey, the energy storage capacity is calculated by the proposed calculating method.

Keywords – electric bus; wireless power transfer (WPT); supercapacitor (SC); hybrid energy storage

I. INTRODUCTION

Internal combustion engines will cause environmental problems, such as air pollution and global warming, while the operation of an electric motor is zero emission [1]. Therefore, compared with traditional buses, electric buses have more advantages. At present, the inconvenience of traditional wired charging mode and the energy storage problem limit the development of electric vehicles (EVs) including electric buses [2].

For the inconvenience of traditional wired charging mode, the applications of wireless power transfer (WPT) technology to EVs [3] and railway vehicles [4] have been studied in recent years. The wireless charging mode is convenient and without spark or electric shock danger. Therefore, in view of the inconvenience of electric bus traditional wired charging mode, wireless charging mode is a solution with prospects for development. As shown in Fig. 1, on bus route, there are some stopping locations such as bus stops and traffic lights intersections. The short stopping time can be used to charge the bus by wireless charging mode. On the premise of guaranteeing the required driving mileage, by frequent wireless charging, the capacity of energy storage device is reduced and the effective utilization of energy is improved. Electric energy can be conveniently and efficiently delivered to the bus by the wireless charging mode, meanwhile, the storage mode of the electric energy also needs to be considered.
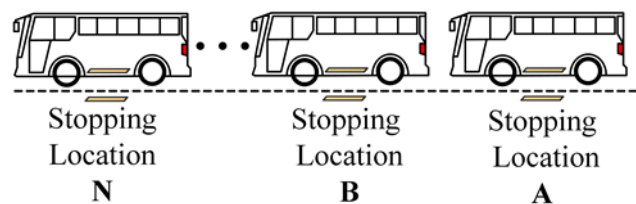

Fig. 1: Diagram of the stopping locations on bus route

For the electric energy storage problem, batteries are suitable to support the progress of EVs because of the high energy density and mobility of batteries [1]. However, the performance and life of batteries are usually rapidly degraded due to frequent high current charging and discharging. Compared with battery [5]-[6], supercapacitor (SC) has higher power density and longer lifetime [6]. Thus, SC is suitable for the frequent wireless charging such as the 3-kW wireless power transfer system for sightseeing car in [7]. In summary, for the electric bus being wireless charged frequently, there are drawbacks in using battery only. And combining the advantages and disadvantages of the above two energy storage modes, it is more appropriate to use the SC-battery hybrid energy storage mode for electric buses, which are heavy duty passenger vehicles [8]. For SC-battery hybrid energy storage mode, it is important to select their appropriate capacities. A calculating method for hybrid energy storage capacity is proposed in this paper. Moreover, the paper proposes the idea that electric buses could be wirelessly charged during the short stopping time at the stopping locations on bus route. However, in order to meet the demand, which is making electric buses fully charged at short notice, it is essential to increase the output power level of WPT system. Therefore, a 100kW WPT charging system is built in the paper.

The concept map of the electric bus wireless charging system with SC-battery hybrid energy storage in this paper is illustrated in Fig. 2. As shown in Fig. 2, after the power distribution, the transmitting coil is powered by the AC-DC-DC-AC power supply. Then the electric energy is transmitted to the receiving coil through electromagnetic coupling. The electric energy received by the receiving coil is used to charge the SC-battery hybrid energy storage device after the rectifying filter. The rest sections of this paper are organized as follows: Section II analyses the equivalent circuit model of the WPT system with SC and battery load. On the basis of the analysis of Section II, the electric bus wireless charging system with SC-battery hybrid energy storage is designed in Section III. The

calculating method for hybrid energy storage capacity is also elaborated in Section III. Section IV implements the electric bus wireless charging system designed in Section III. By using the calculating method, the hybrid energy storage capacity is calculated according to the experimental results and the bus energy consumption survey. Finally, the conclusion is shown in Section V.
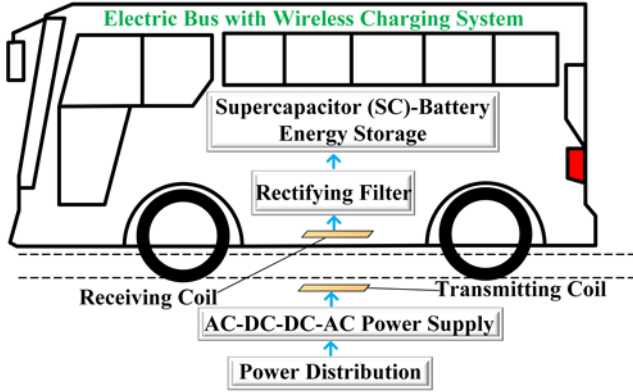

Fig. 2: The concept map of electric bus wireless charging system with SC-battery hybrid energy storage

II. EQUIVALENT CIRCUIT MODEL OF THE WPT SYSTEM WITH SC-BATTERY LOAD

As shown in Fig. 3, by replacing the resistance load of the mutual inductance circuit model in [9] with the SC's classical equivalent circuit model [10] and the simplified battery model [11], the equivalent circuit model of the WPT system with SC and battery is obtained.
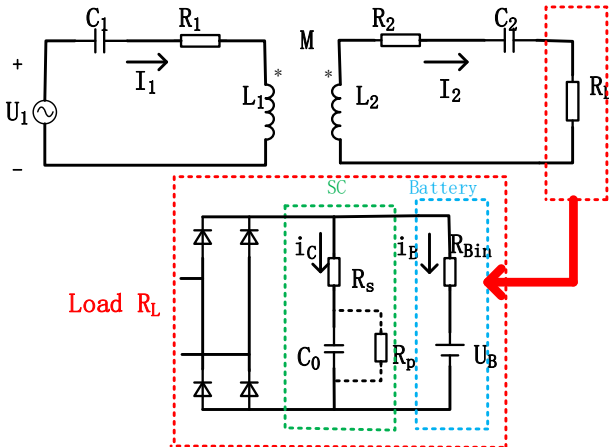

Fig. 3: The equivalent circuit model of the WPT system with supercapacitor (SC) and battery loads

In Fig. 3, u_1 is the voltage of high frequency AC power supply; U_o is the voltage of the load; i_1 and i_2 are the currents of transmitting and receiving coils, respectively; L_1 and L_2 are the inductances of transmitting and receiving coils, respectively; R_1 and R_2 are the equivalent series resistances of transmitting and receiving coils, respectively; series capacitances C_1 and C_2 are the resonant capacitances; M is the mutual inductance of transfer coils; R_s, C_o, R_p and u_{co} are the equivalent series resistance, the ideal capacitance value, the equivalent parallel resistance and the capacitance voltage of SC, respectively; u_B and R_{Bin} are the ideal battery voltage and the battery equivalent internal resistance, respectively; R_{CL} is the equivalent resistance of SC; R_{BL} is the equivalent resistance of battery; R_L is the equivalent resistance of SC-battery loads and rectifier circuit; i_C is the

current flowing through the branch of SC; i_B is the current flowing through the branch of battery.

A. Mutual Inductance Circuit Model of WPT System

According to Kirchhoff's Voltage Law (KVL) and Fig. 3, the mutual inductance circuit relation formula of series resonant WPT system can be written into:

$$\begin{cases} u_1 = (R_1 + j\omega L_1 + \dfrac{1}{j\omega C_1})i_1 - j\omega M i_2 \\ j\omega M i_1 - (R_2 + j\omega L_2 + \dfrac{1}{j\omega C_2} + R_L)i_2 = 0 \end{cases} \quad (1)$$

where $\omega = 2\pi f$ with f being the resonant frequency.

When transmitting coil and receiving coil are identical, i.e. $L_1 = L_2 = L$, $R_1 = R_2 = R$, $C_1 = C_2 = C$, and the resonant angle frequency $\omega = 1 / (LC)^{\wedge}(1/2)$, Equation (1) becomes:

$$\begin{cases} u_1 = Ri_1 - j\omega M i_2 \\ j\omega M i_1 - (R + R_L)i_2 = 0 \end{cases} \quad (2)$$

According to (2), input power P_{in}, output power P_{out} and transfer efficiency η can be written into:

$$P_{in} = u_1 i_1 = \frac{(R + R_L)u_1^2}{R(R + R_L) + (\omega M)^2} \quad (3)$$

$$P_{out} = i_2^2 R_L = \frac{u_1^2 (\omega M)^2 R_L}{[R(R + R_L) + (\omega M)^2]^2} \quad (4)$$

$$\eta = \frac{P_{in}}{P_{out}} = \frac{R_L}{(R + R_L)[1 + \dfrac{R(R + R_L)}{(\omega M)^2}]} \quad (5)$$

Unlike the pure resistance load in [16], R_L is the equivalent resistance of SC-battery load, thus R_L needs to be analyzed.

B. SC Load

The effects of the SC's equivalent parallel resistance R_p can be neglected for transient capacitor discharges on the order of a few seconds to a few minutes [10]. In this paper, the wireless charging system is designed to make use of the short time at each stopping location on bus route to charge the electric bus. Therefore, only the equivalent series resistance R_s and the ideal capacitance C_o are analyzed [7].

Assuming that the load voltage U_o is constant and the charging time is t, the current and the voltage of SC can be denoted by $i_C(t)$ and $u_{co}(t)$, respectively. By KVL, it can be obtained that:

$$U_o(t) = i_C(t)R_s + u_{co}(t) \quad (6)$$

The changes during the charging process can be expressed as:

$$\begin{cases} U_o(0) = i_C(0)R_s + u_{co}(0) \\ U_o(t) = i_C(t)R_s + u_{co}(t) \end{cases} \quad (7)$$

The change of the SC's voltage during the whole charging process (from 0 to t s) is denoted by ΔU_c, i.e. $\Delta U_c = u_{co}(t) - u_{co}(0)$. According to (7), $i_C(t)$ can be written into:

$$i_C(t) = i_C(0) - \frac{\Delta U_c}{R_s} \quad (8)$$

And another expression of $i_C(t)$ is:

$$i_C(t) = C_o \frac{du_{co}}{dt} = C_o \frac{\Delta U_c}{t} \quad (9)$$

According to (8) and (9), ΔU_c can be written into:

$$\Delta U_c = i_C(0) \frac{R_s t}{C_o R_s + t} \quad (10)$$

Therefore, according to (8) and (10), the SC's equivalent resistance, i.e. R_{CL} can be written into:

$$R_{CL} = \frac{U_o}{i_C(t)} = \frac{U_o}{i_C(0)} (1 + \frac{t}{C_o R_s}) \quad (11)$$

The initial current $i_C(0)$ can be written into:

$$i_C(0) = \frac{U_o - u_{co}(0)}{R_s} \quad (12)$$

where $u_{co}(0)$ is the initial voltage of SC. By substituting (12) into (11), it can be obtained that:

$$R_{CL} = \frac{U_o}{U_o - u_{co}(0)} (R_s + \frac{t}{C_o}) \quad (13)$$

It can be seen from (13) that R_{CL} has a dynamic change t/C_o.

C. Battery Load

In Fig. 3, the current flowing through the battery branch, i.e. i_B can be written into:

$$i_B = \frac{U_o - u_B}{R_{Bin}} \quad (14)$$

Thus, the equivalent resistance of battery, i.e. R_{BL} can be written into:

$$R_{BL} = \frac{U_o}{i_B} = \frac{U_o}{U_o - u_B} R_{Bin} \quad (15)$$

where u_B is constant under ideal condition.

In summary, the equivalent resistance of SC-battery loads, i.e. R'_L can be written into:

$$R'_L = \frac{R_{CL} R_{BL}}{R_{CL} + R_{BL}} = \frac{U_o}{\dfrac{U_o - u_{co}(0)}{R_s + \dfrac{t}{C_o}} + \dfrac{U_o - u_B}{R_{Bin}}} \quad (16)$$

$$R_L = \frac{8}{\pi^2} R'_L \quad (17)$$

As shown in formula (17), the relationship between R_L and R'_L is remarkable, which is established with uncontrolled rectifier circuit. In R'_L, there is a dynamic change caused by SC. According to (4), when R_L is known, the output power P_{out} can be adjusted by changing the value of u_1. Thus, the dynamic change should be taken into account in the subsequent wireless charging system design.

III. Design of the Electric Bus Wireless Charging System with SC-Battery Hybrid Energy Storage

A. Overall System Design

The design block diagram of the electric bus wireless charging system with SC-battery hybrid energy storage is illustrated in Fig. 4. The system is divided into two parts: the transmitting part and the receiving part. The transmitting part is installed at each stopping location on bus route. The receiving part is installed on the electric bus.

As shown in Fig. 4, the DC voltage U_{d1} obtained by rectifying filter is input into the DC chopper. The inverter converts the output DC voltage of the DC chopper into high AC frequency voltage. Then the high frequency AC voltage is input into the transmitter of magnetically coupled resonant circuit. The resonant capacitor C_1 and the transmitting coil L_1 form the resonant circuit of the transmitter. Electric energy is sent to the receiver by electromagnetic coupling. The resonant capacitor C_2 and the receiving coil L_2 form the resonant circuit of the receiver. By the high-frequency rectifying and filtering circuit, the electric energy is converted into the DC voltage, which is used to charge the SC-battery hybrid energy storage device.
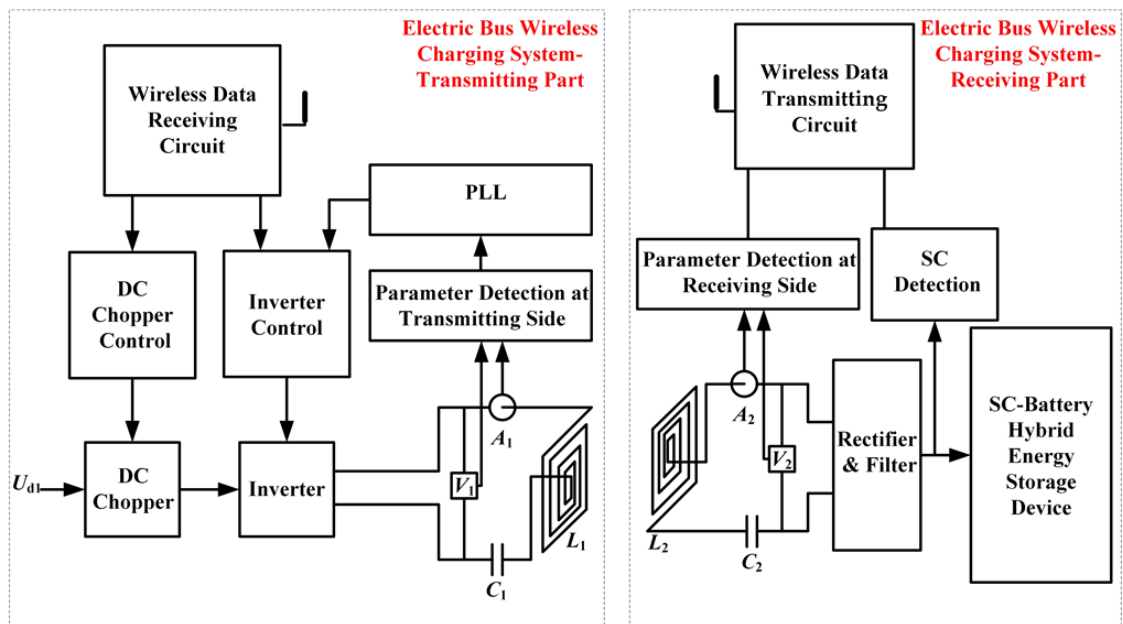

Fig. 4: The design block diagram of electric bus wireless charging system with SC-battery hybrid energy storage
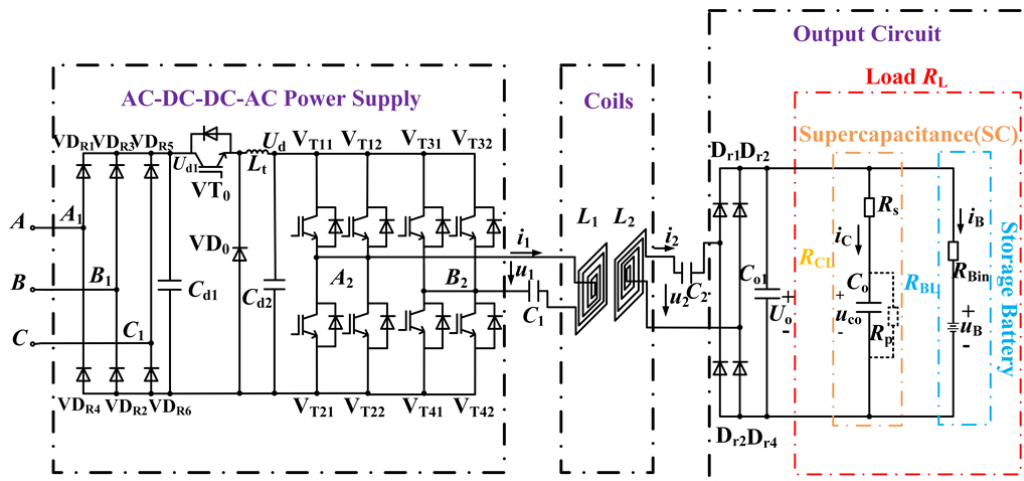
Fig. 5: Diagram of electric bus wireless charging system circuit

As shown in Fig. 4, the parameter detection at transmitting side is to detect inverter output voltage and current. The detected voltage and current will be used for PLL frequency tracking. The parameter detection of receiving side is divided into rectifier input voltage and current detection and SC detection. SC detection is used to obtain the required voltage and current of SC. The detected parameters of receiving side are sent to transmitting side by wireless communication circuit.

The system control includes DC chopper circuit control and inverter frequency tracking control. 1) DC chopper circuit control: In the circuit model analysis of Section 2, R_L has a dynamic change. Thus, the SC detection circuit is added to the system. After the SC detection, the detected data is sent to the wireless data receiving circuit by the wireless data transmitting circuit, and the received data is processed. According to the required voltage and current of SC, the output power is regulated by the control of the DC chopper circuit. 2) Inverter frequency tracking control: When the parameters of the resonant circuit are changed, the PLL frequency tracking circuit automatically tracks the resonant frequency.

B. Design of the Electric Bus Wireless Charging System Circuit

The system circuit is designed according to the overall system design. The diagram of electric bus wireless charging system circuit is illustrated in Fig. 5. The system circuit consists of three parts: 1) AC-DC-DC-AC power supply; 2) coils and related resonant circuits; 3) output circuit.

1) AC-DC-DC-AC power supply

The three-phase rectifier bridge (VD_{R1}-VD_{R6}) and the filter capacitor C_{d1} are used to convert A, B, and C three-phase AC voltage into the DC voltage U_{d1}. And U_{d1} is input into the Buck circuit (VT_0, VD_0, Cd_2). By the inverter circuit, the output voltage of Buck circuit, i.e. U_d is converted into the high frequency AC voltage, which corresponds to u_1 in Fig. 3. The power level of the wireless charging system in this paper is very large. In order to sustain the rated large current, IGBT parallel connection needs to be adopted.

2) Coils and related resonant circuits

The parameters of the symmetrical square coils used in this paper are as follows: the average side lengths of both coils are 0.85 m; the turn numbers of both coils are 10; the thickness of the magnetic conductor is 5 mm; the side length of the square magnetic conductor is 1.2 m.

To facilitate the design of the related resonant capacitors, finite element analysis software is used to simulate the coils. The coils simulation model is illustrated in Fig. 6. The self-inductance ($L_1 = L_2 = 4.5629 \times 10^{-4}$ H) and the mutual inductance ($M = 3.9156 \times 10^{-5}$ H) are obtained by the simulation.
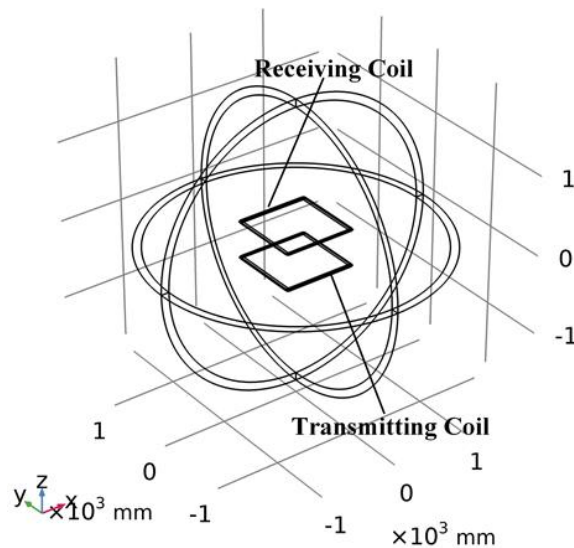

Fig. 6: The coils simulation model

3) Output circuit

By the high frequency rectifier (D_{r1}-D_{r4}) and the filter capacitor (C_{o1}), the high frequency AC output of the receiving coil is converted into the DC voltage, which corresponds to U_o in Fig. 3. And U_o charges the SC-battery hybrid energy storage device.

According to the above design of the system and the circuit, the electric bus wireless charging system can be implemented. But for the whole system, the capacity selection of hybrid energy storage device is equally important. Under the premise of continuous and reliable driving, determining the appropriate capacity of hybrid energy storage device can greatly reduce the cost of system.

C. Calculating Method for Hybrid Energy Storage Capacity

This calculating method is for the pure electric buses with SC-battery hybrid energy storage. The long-term storage device is battery, and the short-term storage device is SC.

The time for a bus going to and fro on its route one or more times is recorded as t_{all}. And the related data is recorded at a regular time interval Δt. Then the number of recording points n is $t_{all}/\Delta t$. The related data is recorded as follows:

There is wireless communication between the transmitting side and the receiving side of the wireless charging system designed in this paper. Therefore, historical WPT received power $P_{WPT}(t_i)$ can be recorded by analyzing the data of the system transmitting side installed at each stopping location on bus route. And historical actual demand power $P_{bus}(t_i)$ are recorded at each recording point, where $i=1, 2, 3..., n$. Historical supply-demand mismatch power $P_\Delta(t_i)$ and historical average supply-demand mismatch power $P_{\Delta avg}(t)$ are obtained by (18) and (19).

$$P_\Delta(t_i) = P_{WPT}(t_i) - P_{bus}(t_i) \tag{18}$$

$$P_{\Delta avg}(t) = \frac{\sum_{i=1}^{n} P_\Delta(t_i)}{n} \tag{19}$$

By $P_{WPT}(t_i)$, $P_{bus}(t_i)$, $P_\Delta(t_i)$, and $P_{\Delta avg}(t)$, the capacity of SC-battery hybrid energy storage device is calculated as follows:

1)Battery (long-term) energy storage capacity

Assuming that the maximum of the sum of any q consecutive $P_\Delta(t_i)$ is $max(\sum P_\Delta(t_i))$, then the battery energy storage capacity E_1 is the time integral of the corresponding q consecutive $P_\Delta(t_i)$, where $1 \le q \le n$. Moreover, in order to protect the battery from over discharge and ensure the stability of power supply, it is necessary to keep E_1 larger than calculated value.

2)SC (short-term) energy storage capacity

Fast Fourier Transform (FFT): By FFT and historical supply-demand mismatch power $P_\Delta(t_i)$, historical supply-demand mismatch power of frequency domain, i.e. $P_\Delta(f_i)$ are obtained. Due to the character of FFT, only data within half of the sampling frequency are analyzed. Then $P_\Delta(f_i)$ are converted into periodic supply-demand mismatch power $P_\Delta(T_i)$, where $i =1, 2, 3..., n / 2$ and $T = 1 / f$.

Standardization: According to (20), total supply-demand mismatch power $P_{\Delta all}$ is obtained. Then according to (21), periodic supply-demand mismatch power $P_\Delta(T_i)$ is standardized.

$$P_{\Delta all} = \sum_{i=1}^{n/2} P_\Delta(T_i) \tag{20}$$

$$P'_\Delta(T_i) = \frac{P_\Delta(T_i)}{P_{\Delta all}} \tag{21}$$

where $i = 1, 2, 3..., n / 2$.

Accumulation: Accumulated value of supply-demand mismatch power, i.e. $P''_\Delta(T_k)$ are calculated as shown in (22).

$$P''_\Delta(T_k) = \sum_{i=k}^{n/2} P'_\Delta(T_i) \tag{22}$$

where $k=1, 2, 3..., n/2$. Then a continuous function curve of $P''_\Delta(T_k)$ is obtained.

Selection of critical percentage: In logarithmic coordinates, when the function value decreases from the maximum to $20\log(1/2)^{1/2}$ of the maximum, the function value corresponding to the continuous function is the critical percentage k_p. A corresponding $T_k(k_p)$ is obtained by finding the $P''_\Delta(T_k)$ closest to k_p. The period length less than $T_k(k_p)$ can be considered to be buffered by energy storage device.

Capacity calculation: The SC energy storage capacity E_2 is the product of the corresponding $T_k(k_p)$ and historical average supply-demand mismatch power $P_{\Delta avg}(t)$, i.e. $E_2 = P_{\Delta avg}(t) \times T_k(k_p)$.

IV. IMPLEMENTATION OF THE WIRELESS CHARGING SYSTEM

A. EXPERIMENT RESULTS OF THE WIRELESS CHARGING SYSTEM

In order to facilitate the power design of the wireless charging system and the calculation for energy storage capacity, the historical actual demand power $P_{bus}(t_i)$ of a bus were recorded. The $P_{bus}(t_i)$ is illustrated in Fig. 7.
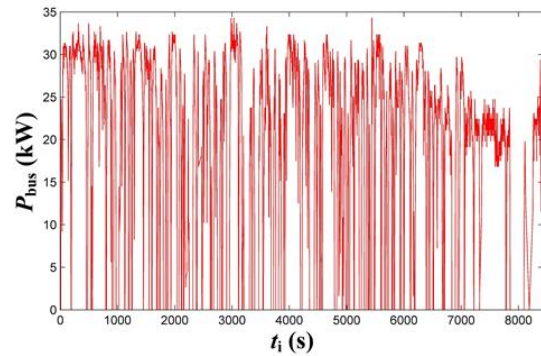

Fig. 7: Historical actual demand power $P_{bus}(t_i)$

As shown in Fig. 7, t_{all} is 8427 s, and the regular time interval Δt is 1 s. Then the number of recording points n is 8427. Within 8427 s, the bus consumes 42 kW·h. If the bus is charged at 80 kW when it stops ($P_{bus}(t_i) = 0$ kW), the charging energy of the bus within 8427 s is 45 kW·h, which can meet the demand. Therefore, in consideration of system transfer efficiency, a wireless charging system with 100 kW input power is implemented as shown in Fig. 8.

Fig. 8: Diagram of the wireless charging experiment device with 100 kW input power

In Fig. 8, the frequency tracking range of the 100 kW high-frequency AC-DC-DC-AC power supply is 30–60 kHz. Both the transmitting coil and the receiving coil are square planar coils. And the average side lengths of both coils are 0.85 m.

The experimental results are shown in Table 1, where U_1 is the input voltage; I_1 is the input current; P_1 is the input power; U_2 is the output voltage; I_2 is the output current; P_2 is the output power; h is the transfer distance; f is the frequency of the power supply; η is the transfer efficiency.

As shown in Table 1, when the transfer distance h is 0.45 m, the output power P_2 can be 80.2 kW, which satisfies the power demand, at the efficiency of 89.6%.

Table 1: Experimental Result of the Wireless Charging System

U_1 (V)	I_1 (A)	P_1 (kW)	U_2 (V)	I_2 (A)	P_2 (kW)	h (m)	f (kHz)	η (%)
500.3	125.2	62.63	476.4	120.7	57.5	0.3	46.9	91.8
507.3	150.0	76.12	523.2	131.6	68.9	0.4	43.5	90.5
515.7	173.5	89.5	564.7	142.4	80.2	0.45	42.7	89.6

B. Calculation of the System Hybrid Energy Storage Capacity

According to the recorded $P_{bus}(t_i)$ and the design of Section III, a 100 kW wireless charging system for electric bus is implemented. On the basis of this wireless charging system, the SC (short term) and battery (long term) energy storage capacities are calculated by the calculating method proposed in Section III.

If the wireless charging system in this paper is used, the electric bus can be wirelessly charged with power of 80 kW at the stopping locations on bus route. In other words, when $P_{bus}(t_i) = 0$ kW, $P_{WPT}(t_i) = 80$ kW. According to Fig. 7, $P_{WPT}(t_i)$ can be obtained as shown in Fig. 9.
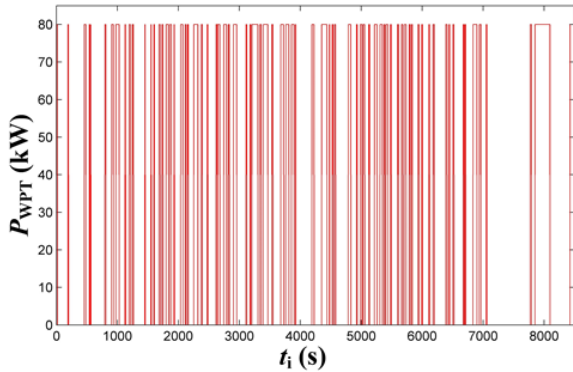

Fig. 9: Historical WPT received power $P_{WPT}(t_i)$

According to (19), Fig. 7, and Fig. 9, the historical supply-demand mismatch power $P_\Delta(t_i)$ can be obtained as shown in Fig. 10. And in Fig. 10, the maximum of the sum of any q consecutive $P_\Delta(t_i)$, i.e. $\max(\sum P_\Delta(t_i))$ is 36601 kW. The corresponding recording points n are 1682–5838 with q being 4157.

Therefore, the battery (long term) energy storage capacity E_1 can be written into:

$$E_1 = \int_{t_{1682}}^{t_{5838}} P_\Delta(t_i) \tag{23}$$

And E_1 is calculated to be 10.14 kW·h.

Next, the SC (short term) energy storage capacity E_2 is calculated. By FFT and the historical supply-demand mismatch power in Fig. 10, i.e. $P_\Delta(t_i)$, the historical supply-demand mismatch power of frequency domain, i.e. $P_\Delta(f_i)$ are obtained as shown in Fig. 11. In Fig. 11, only the data within half of the sampling frequency are analyzed. Then $P_\Delta(f_i)$ are converted into the periodic supply-demand mismatch power $P_\Delta(T_i)$ as shown in Fig. 12. In Fig. 12, to make the display more intuitive, the horizontal axis is transformed to logarithmic coordinates.
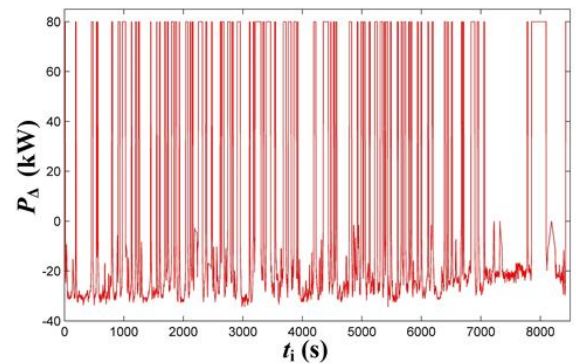

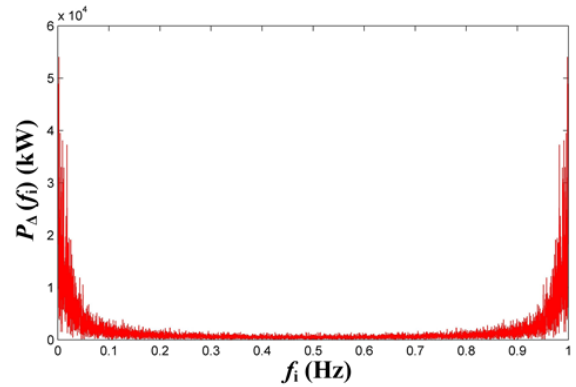Fig. 10: Historical supply-demand mismatch power $P_\Delta(t_i)$

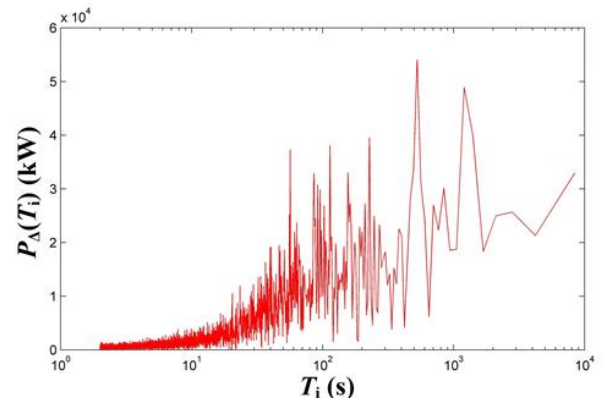Fig. 11: Historical supply-demand mismatch power of frequency domain $P_\Delta(f_i)$

Fig. 12: Periodic supply-demand mismatch power $P_\Delta(T_i)$

According to (20), the total supply-demand mismatch power $P_{\Delta all}$ is obtained. And by $P_{\Delta all}$ and (21), $P_\Delta(T_i)$ is standardized.

Then, the accumulated value of supply-demand mismatch power $P''_\Delta(T_k)$ are calculated according to (22). The continuous function curve of $P''_\Delta(T_k)$ is obtained as shown in Fig. 13. the critical percentage $k_p = 0.293 \approx 0.3$. Then the corresponding $T_k(k_p)$ $(T_k(k_p) = 61$ s) is obtained by finding the $P''_\Delta(T_k)$ closest to 0.3. Therefore, the SC (short term) energy storage capacity $E_2 = P_{\Delta avg}(t) \times T_k(k_p) = 0.02$ kW·h.
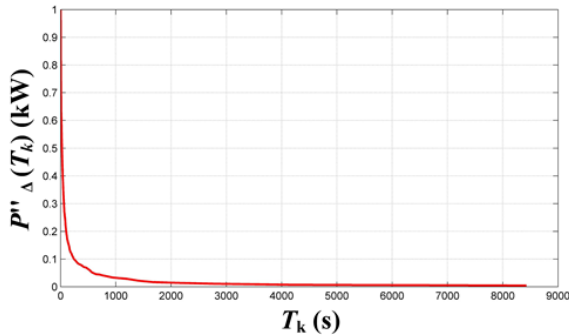

Fig. 13: Accumulated value of supply-demand mismatch power $P''_\Delta(T_k)$

V. CONCLUSION

In this paper, for the application background of electric buses being wirelessly charged during the short stopping time at the stopping locations on bus route, a set of 100 kW electric bus wireless charging system is designed and implemented. When the transfer distance h is 0.45 m, the output power P_2 can be 80.2 kW, which satisfies the power demand, at the efficiency of 89.6%. And the calculating method for hybrid energy storage capacity is used to calculate the capacity.

In this paper, considering the present experimental condition limit, SC-battery load is replaced by resistances. The charging problems of SC-battery, such as the different working voltage range and power distribution, will be taken into account in the further research using actual SC and battery and corresponding converters circuits. In the experiment of the further research, the SC and battery with the calculated energy storage capacity will be used and the system performance will be tested.

ACKNOWLEDGMENT

REFERENCES

[1] J. Hu, F. Lu, and C. Zhu et al.: Hybrid energy storage system of an electric scooter based on wireless power transfer. IEEE Trans. Ind. Inform. 14(9), 4169–4178 (2018).

[2] X. Mou, O. Groling, and H. Sun: Energy-efficient and adaptive design for wireless power transfer in electric vehicles. IEEE Trans. Ind. Electron. 64(9), 7250–7260 (2016).

[3] R. Tavakoli and Z. Pantic: Analysis, design, and demonstration of a 25-kW dynamic wireless charging system for roadway electric vehicles. IEEE J. Emerg. Sel. Top. Power Electron. 6(3), 1378–1393 (2018).

[4] J. H. Kim, B. S. Lee, and J. H. Lee et al.: Development of 1-MW inductive power transfer system for a high-speed train. IEEE Trans. Ind. Electron. 62(10), 6242–6250 (2015).

[5] J. M. Blanes, R. Gutiérrez, and A. Garrigos et al.: Electric vehicle battery life extension using ultracapacitors and an FPGA controlled interleaved buck–boost converter. IEEE Trans. Power Electron. 28(12), 5940–5948 (2013).

[6] F. Naseri, E. Farjah, and T. Ghanbari: An efficient regenerative braking system based on battery/supercapacitor for electric, hybrid, and plug-in hybrid electric vehicles with BLDC motor. IEEE Trans. Veh. Technol. 66(5), 3724–3738 (2017).

[7] Z. Li, C. Zhu, and J. Jiang et al.: A 3-kW wireless power transfer system for sightseeing car supercapacitor charge. IEEE Trans. Power Electron. 32(5), 3301–3316 (2017).

[8] J. M. Miller, and A. Daga: Elements of wireless power transfer essential to high power charging of heavy duty vehicles. IEEE Trans. Transp. 1(1), 26–39 (2015).

[9] Y. Dong, W. Lu, and Y. Liu et al.: Optimal study of resonant wireless charging coils for electric vehicles. in Proceedings of the 2018 21st International Conference on Electrical Machines and Systems (ICEMS). IEEE. Jeju, South Korea, 7–10 (2018).

[10] R. L. Spyker and R. M. Nelms: Classical equivalent circuit parameters for a double-layer capacitor. IEEE Trans. Aerosp. Electron. Syst. 36(3), 829–836 (2000).

[11] Q. Xu, J. Xiao, and X. Hu et al.: A decentralized power management strategy for hybrid energy storage system with autonomous bus voltage restoration and state-of-charge recovery. IEEE Trans. Ind. Electron. 64(9), 7098–7108 (2017).

Author Index

Submission Details

Only online submission will be accepted. Please first register and submit online. The paper is in double-column and is similar to most IET or IEEE journal formats. There is no page limit. Any number of pages of more than 6 will be subjected to an additional charge.

The paper guidelines can be downloaded using the link: http://perc.polyu.edu.hk/apejournal/

Any queries, please contact Prof. Eric Cheng, Publishing Director of APEJ, Dept. of Electrical Engineering, The Hong Kong Polytechnic University, Hung Hom, Hong Kong. Email: eeecheng@polyu.edu.hk   Fax: +852-2330 1544

Any secretarial support and production related matters, please contact Dr. James Ho, Power Electronics Research Centre, The Hong Kong Polytechnic University, Hung Hom, Hong Kong. Email: eeapej@polyu.edu.hk   Tel: +825-3400 3348 Fax: +852-3400 3343

Publication Details

The journal will be published 2-3 times a year. The first issue was published in 2007. Response time for paper acceptance is within 3 months.

Financial Charge

All the accepted papers will be printed without charge for 6 or less pages. An additional page charge is HK$100 per page. A hardcopy of the journal will be posted to the corresponding author free of charge. Additional copies of the journal can be purchased at HK$200 each. The charge includes postage and packing.

All Chinese Papers will be subjected to a translational fee of HK$350 per page. It will be charged when the paper is accepted for publication.

Advertising

Advertisement is welcome. Full page advertisement is HK$1000. For colour advertisements, the amount is doubled. All the advertisements will be both posted online in the journal website and hardcopy of the journal.

For advertising enquires and details, please contact Ms. Anna Chang, eeapej@polyu.edu.hk.

Tel: +852-3400 3348, Fax: +852-3400 3343

For payment, please send your cheque, payable to 'The Hong Kong Polytechnic University, address to Ms. Kit Chan, Secretary of APEJ, Dept. of Electrical Engineering, The Hong Kong Polytechnic University, Hung Hom, Hong Kong.'